ADAPTIVE OPTICS IMAGING OF IRAS 18276−1431: A BIPOLAR PREPLANETARY NEBULA WITH CIRCUMSTELLAR "SEARCHLIGHT BEAMS" AND "ARCS"

C. Sánchez Contreras,[1] D. Le Mignant,[2] R. Sahai,[3] A. Gil de Paz,[4] and M. Morris[5]

ABSTRACT

We present high angular resolution images of the post-AGB nebula IRAS 18276−1431 (also known as OH 17.7-2.0) obtained with the Keck II adaptive optics (AO) system in its natural guide star (NGS) mode in the K_p, L_p, and M_s near-infrared bands. We also present supporting optical F606W and F814W *HST* images as well as interferometric observations of the ^{12}CO $J = 1–0$, ^{13}CO $J = 1–0$, and 2.6 mm continuum emission with OVRO. The envelope of IRAS 18276−1431 displays a clear bipolar morphology in our optical and NIR images with two lobes separated by a dark waist and surrounded by a faint $4.5'' \times 3.4''$ halo. Our K_p-band image reveals two pairs of radial "searchlight beams" emerging from the nebula center and several intersecting, arclike features. From our CO data we derive a mass of $M > 0.38(D/3 \text{ kpc})^2 M_\odot$ and an expansion velocity $V_{\exp} = 17$ km s^{-1} for the molecular envelope. The density in the halo follows a radial power law $\propto r^{-3}$, which is consistent with a mass-loss rate increasing with time. Analysis of the NIR colors indicates the presence of a compact central source of $\sim 300–500$ K dust illuminating the nebula in addition to the central star. Modeling of the thermal IR suggests a two-shell structure in the dust envelope: (1) an outer shell with inner and outer radius $R_{\rm in} \sim 1.6 \times 10^{16}$ and $R_{\rm out} \gtrsim 1.25 \times 10^{17}$ cm, dust temperature $T_{\rm dust} \sim 105–50$ K, and a mean mass-loss rate of $\dot{M} \approx 10^{-3} M_\odot$ yr^{-1}; and (2) an inner shell with $R_{\rm in} \sim 6.3 \times 10^{14}$ cm, $T_{\rm dust} \sim 500–105$ K, and $\dot{M} \sim 3 \times 10^{-5} M_\odot$ yr^{-1}. An additional population of big dust grains (radius $a \gtrsim 0.4$ mm) with $T_{\rm dust} = 150–20$ K and mass $M_{\rm dust} = (0.16–1.6) \times 10^{-3}(D/3 \text{ kpc})^2 M_\odot$ can account for the observed submillimeter and millimeter flux excess. The mass of the envelope enclosed within $R_{\rm out} = 1.25 \times 10^{17}$ cm derived from SED modeling is $\sim 1(D/3 \text{ kpc})^2 M_\odot$.

Subject headings: circumstellar matter — infrared: stars — instrumentation: adaptive optics — ISM: jets and outflows — planetary nebulae: general — stars: AGB and post-AGB — stars: imaging — stars: mass loss

1. INTRODUCTION

In recent years, $\sim 0.1''$ resolution imaging with the *Hubble Space Telescope* (*HST*) has provided many new insights into the evolution from the asymptotic giant branch (AGB) to the phase of planetary nebula (PN). This transition, which takes place through the intermediate short-lived ($\sim 10^3$ yr) stage of preplanetary nebula (PPN), is characterized by dramatic changes of the nebular morphology and kinematics: the spherical, slowly expanding ($V_{\exp} \sim 15$ km s^{-1}) AGB circumstellar envelope (CSE) develops clear departures from sphericity and fast ($\gtrsim 100$ km s^{-1}) outflows directed in opposing directions along one or more axes. Although there is no consensus yet for what causes this spectacular metamorphosis, fast jetlike winds have been hypothesized to play an important role (see, e.g., a recent review by Balick & Frank 2002). In light of the many structural details revealed by *HST* data, e.g., the multiple lobes and the high degree of point symmetry of outflows observed in most young PNs and PPNs, Sahai & Trauger (1998) hypothesized that fast collimated outflows are the primary agent for setting the stage in the shaping of PNs, rather than a preexisting equatorial density enhancement in the AGB CSEs, as assumed in the popular generalized interacting stellar winds model (Balick 1987). These outflows carve out a complex imprint within the AGB CSE producing and shaping the fast, bipolar lobes observed in most PPNs and PNs.

In order to study the poorly known mass-loss processes mediating the AGB-to-PN transition, we have obtained 1.6–4.7 μm images of PPNs with the Keck adaptive optics (AO) system (Sánchez Contreras et al. 2006). This forms part of our extensive, multiwavelength studies of PPNs, which also include optical/NIR *HST* imaging and optical spectroscopy (Sahai & Sánchez Contreras 2004) and millimeter wavelength interferometry (Sánchez Contreras & Sahai 2004). Progress in our understanding of post-AGB evolution requires high spatial resolution because most PPNs are very small in angular extent ($\lesssim 5''$) and exhibit rich structure at a scale $\lesssim 0.1''$, and because the shaping mechanism operates very close to the central star, $\lesssim 10^{16}$ cm (Balick & Frank 2002; Sánchez Contreras & Sahai 2001). Also, observing at long wavelengths is desirable, since the dusty CSEs of most post-AGB objects are very optically thick.

In this paper we present K_p, L_p, and M_s AO images of the PPN IRAS 18276−1431, together with optical Wide Field and Planetary Camera 2 (WFPC2) *HST* and interferometric 2.6 mm (CO line and continuum emission) data, which have helped our understanding of the complex structure of this object. Observational details and results are described in §§ 2 and 3. The analysis of the NIR and optical colors to derive the dust extinction toward the central star and the nature of the illuminating source are presented in §§ 4 and 5. Structural components and physical parameters (mass, mass-loss rate, and dust temperature) of IRAS 18276−1431 are discussed in §§ 6 and 7. The formation and evolution of IRAS 18276−1431 is described in § 8. Our main conclusions are summarized in § 9.

[1] Departamento de Astrofísica Molecular e Infrarroja, Instituto de Estructura de la Materia, CSIC, Madrid, Spain.
[2] W. M. Keck Observatory, Kamuela, HI.
[3] Jet Propulsion Laboratory, California Institute of Technology, Pasadena, CA.
[4] Departamento de Astrofísica, Universidad Complutense de Madrid, Madrid, Spain.
[5] Department of Physics and Astronomy, University of California, Los Angeles, CA.

TABLE 1

AO AND *HST* OBSERVATIONS AND PHOTOMETRY OF IRAS 18276−1431

Filter	λ_0 (μm)	$\Delta\lambda$ (μm)	Time (s)	FWHM (mas)	rms (σ) (mJy pixel^{-1})	I_{max} (mJy pixel^{-1})	Flux (mJy)	NE-to-SW Flux Ratio
F606W[a]	0.61	0.123	200	138	4×10^{-6}	3.8×10^{-3}	0.9	4
F814W[a]	0.81	0.149	120	138	1×10^{-5}	1.1×10^{-2}	3.0	3
K_p[b]	2.12	0.351	270	60–65[c]	8×10^{-6}	4.3×10^{-2}	96	1.3
L_p[b]	3.78	0.700	225	80–85[c]	3×10^{-4}	0.29	385	1.4
M_s[b]	4.67	0.241	180	95–100[c]	2×10^{-3}	0.70	781	1.4

[a] *HST* subsampled images: FOV = $35'' \times 35''$; 22.8 mas pixel^{-1}.
[b] Keck AO images: FOV = $10'' \times 10''$; 9.94 mas pixel^{-1}.
[c] Range determined from PSF fitting to several field stars at the same radial distance from the reference star as our target.

1.1. *The Preplanetary Nebula IRAS 18276−1431*

IRAS 18276−1431 (also known as OH 17.7-2.0) is an OH/IR star that has reached the end of its evolution on the AGB and is rapidly evolving to the PN phase. IRAS 18276−1431 displays the classical bimodal spectral energy distribution (SED) observed in PPNs, which is indicative of a detached CSE with relatively cool ($\sim$150 K) dust grains (Le Bertre 1987). The progressive disappearance of H_2O maser emission in IRAS 18276−1431 is consistent with a recent drop of the mass-loss rate from $\dot{M} \gtrsim 10^{-5}$ to well below $\dot{M} = 10^{-7}$ $M_\odot$ yr^{-1} (Engels 2002). The cessation of the large-scale mass loss, indicated by both the disappearance of the H_2O masers and the presence of a detached envelope, is believed to designate the beginning of the post-AGB evolution. The nondetection of SiO masers in IRAS 18276−1431 (Nyman et al. 1998) is also consistent with the post-AGB nature of this object. The central star of IRAS 18276−1431 has a spectral type earlier than $\sim$K5, with an effective temperature in the range $T_{eff} = 4000$–10,000 K and a total luminosity of $L \sim 1.5 \times 10^4$ $(D/4.6 \text{ kpc})^2$ (Le Bertre et al. 1989). This is a confirmation that the object has left the AGB.

Ground-based imaging polarimetry in the J and K near-infrared bands shows an extended, nonspherical scattering envelope around IRAS 18276−1431 (Gledhill 2005). The angular size of the envelope and position angle of its major axis in the J (K) band are $\sim 3'' \times 2''$ and P.A. = $24° \pm 2°$ ($3.9'' \times 3.4''$ and P.A. = $22° \pm 2°$), respectively. The polarized intensity images reveal a clear bipolar morphology and polarization vectors that are mostly aligned perpendicular to the bipolar axis, at P.A. $\approx 23°$. This is typical of scattering in an optically thick envelope, where light escapes preferentially along bipolar cavities (Bains et al. 2003; Gledhill 2005). The axisymmetric scattering models by Gledhill (2005) suggest that the lobes of IRAS 18276−1431 lie very close to the plane of the sky, with an approximate inclination of $i \sim 3°$.

Strong OH maser emission is observed in the equatorial region IRAS 18276−1431 (Bains et al. 2003). This dense, equatorial component is elongated in the direction of P.A. $\sim 110°$, i.e., is approximately perpendicular to the polar cavities, and has inner and outer angular radii of $0.25''$ and $0.85''$, respectively. As discussed by Bains et al. (2003), hornlike features observed in the OH maser position-velocity diagram (see their Fig. 10) probably trace the base of a bipolar outflow very close to the central source. The relative absence of OH masers in the polar regions (compared with the much more intense OH emission observed in the equatorial regions) is consistent with the interpretation of these polar regions as cavities within which the lower gas density fails to generate strong maser emission. These OH maser observations also suggest a large-scale, regular magnetic field of strength $B = +4.6$ mG (1612 MHz) and $B = +2.5$ mG (1667 MHz) in IRAS 18276−1431 that could have played a role in causing the equa-

torially enhanced mass loss in this object. A burst of strongly polarized OH maser emission that could be linked to recent evolutionary changes in the shell has been reported by Szymczak & Gérard (2005).

The distance to IRAS 18276−1431 is uncertain. OH phase-lag measurements indicate a distance in the range $D = 2$–5.4 kpc (Bowers et al. 1983; Herman & Habing 1985). The near-kinematic distance is $D = 4.6$ kpc (Le Bertre et al. 1989). In this paper, we adopt an intermediate value of $D = 3$ kpc.

2. OBSERVATIONS

2.1. *Near-Infrared Natural Guide Star AO Imaging*

We have imaged the dust envelope around the OH/IR star IRAS 18276−1431 through the K_p (2.12 μm), L_p (3.8 μm), and M_s (4.7 μm) filters with the W. M. Keck II 10 m telescope using the NIRC2 Camera (K. Matthews et al. 2007, in preparation) with AO (Wizinowich et al. 2000). IRAS 18276−1431 was observed with AO in its natural guide star (NGS) mode on UT 2005 August 12 at air mass 1.22–1.26. The AO guide star, USN-0755-0509985 ($m_V = 11.0$), is located $23.2''$ south and $0.13''$ east from IRAS 18276−1431. The AO system ran at the speed of 315 Hz with an average intensity per subaperture of 120 counts. The field of view (FOV) and pixel scale of the NIRC2 narrow camera is $10'' \times 10''$ and 9.94 mas pixel^{-1}. The seeing was $0.4''$ in the visible, as measured on the acquisition camera.

The images in the different bands were acquired using a generic 3-position dithering script avoiding the noisiest quadrant of NIRC2 where the number of frames for each position was three in K_p, six in L_p, and six in M_s. The images have been reduced in a standard way. First, we derived a sky frame by computing the filtered median of all frames for each band. Then, each frame was sky-subtracted, flat-fielded, corrected for bad pixels, and shift-and-added in a final image for each observing setup. We also observed the photometric standard 148 S810-A from Leggett et al. (2003) at UT 08:30 in the same region of the sky that we used to derive the photometry zero points for K_p, L_p, and M_s. We have used the magnitude-to-millijansky flux density conversion factors given by Tokunaga & Vacca (2005).

The spatial resolution in the images is nearly diffraction limited for the Keck II telescope in K_p (60–65 vs. 48 mas) and diffraction limited in L_p and M_s (Table 1). The point-spread function (PSF) of our images has the typical elongation resulting from the AO anisoplanatism effect, as expected when the AO guide star is offset from the science target. This effect is seen in the K_p-band images, where the PSF varies from 55 mas near the AO guide star to 75 mas in the most distant imaged stars. This elongation is not seen in L_p and M_s, as the isoplanatic angle becomes much larger ($\geq 50''$). We have used the nearest stars to IRAS 18276−1431 to check the image quality and characterize the PSF in our target
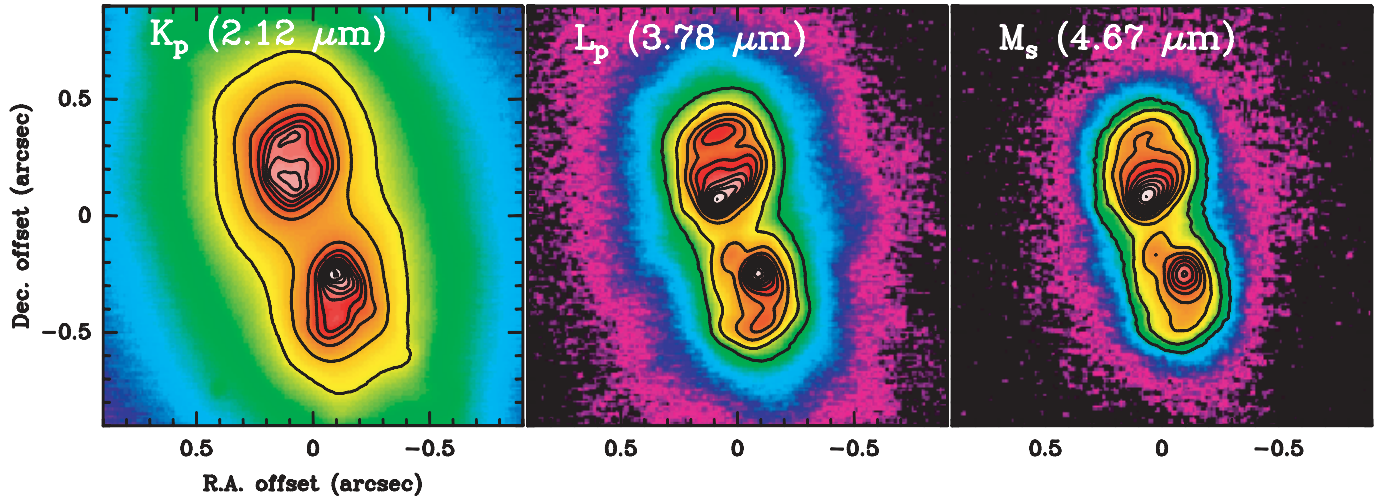
Fig. 1.—AO images of IRAS 18276−1431 in the K_p, L_p, and M_s near-infrared bands. A logarithmic intensity scale, from 3 σ to 95% of the intensity maximum in each image, has been used (see Table 1). Contours are for levels at 5%, and from 10% to 100% of the maximum in each image in 10% steps.

(Table 1). The Strehl ratio (SR) was measured to be 0.16 (0.75) in the K_p (L_p) image, giving a scaled SR of 0.80 in M_s.

2.2. Optical F606W and F814W HST Imaging

IRAS 18276−1431 was imaged on UT date 2002 February 16 (GO/SNAP program 9101) with the 800×800 pixel planetary camera of the WFPC2, which has a plate scale of $0.0456''$ pixel^{-1}, using the F606W ($\lambda = 0.60$ μm, $\Delta\lambda = 0.123$ μm; exposures were 2×5 s and 2×100 s) and F814W ($\lambda = 0.80$ μm, $\Delta\lambda = 0.149$ μm; exposures were 2×3 s and 2×60 s) filters. For both filters, each of the two long-exposure images were dithered relative to each other by about 7.7 pixels to improve the image quality. The standard pipeline-processed images were retrieved from the *HST* archive. The short-exposure images were used to check for saturated pixels in the long-exposure ones, and none were found. The long-exposure images were subsampled by a factor of 2 and then registered to a common reference frame with high precision (i.e., to within ≲0.1 pixel) using field stars. Cosmic-ray removal and averaging was then carried out using the registered images.

2.3. Millimeter-Wavelength Mapping with OVRO

Interferometric mapping of the ^{12}CO $J = 1-0$ and ^{13}CO $J = 1-0$ emission lines at 115 and 110 GHz of IRAS 18276−1431 was carried out using the millimeter interferometer of the Owens Valley Radio Observatory (OVRO)[6] on 2002 September 29, with five antennas and baselines ranging from 18 to 55 m. The units of the digital spectral line correlator were arranged to provide a total bandwidth of 90 MHz ($\sim$234 km s^{-1}) with a channel spacing of 1 MHz (corresponding to $\sim$2.6 km s^{-1}). The 3 mm continuum emission from IRAS 18276−1431 was observed simultaneously using the dual-channel analog continuum correlator, which provided a total bandwidth of 4 GHz (after combining both IF bands). Total duration of the track (including integration time on source and calibrators) was $\sim$6 hr. IRAS 18276−1431 was observed $\pm$2.6 hr around its transit.

The calibration of the data was performed using the MMA software package.[7] Data were gain calibrated in baseline-based mode using the quasar J1833−210, which was observed at regular time intervals of $\sim$20 minutes before and after our target. The quasar

---

3C 273 and the planet Uranus were used as passband and flux calibrators, respectively. The flux of the gain calibrator J1833−210 was estimated to be 2.2 Jy at 115 GHz. Flux calibration errors could range up to 30%.

Reconstruction of the maps from the visibilities was done using the Multichannel Image Reconstruction, Image Analysis and Display (MIRIAD) software. We Fourier transformed the measured visibilities with robust weighting, which is an optimized compromise between natural and uniform weighting, for ^{12}CO and natural weighting for ^{13}CO for S/N optimization. After that, data were cleaned and maps restored. The clean beam for our ^{12}CO (^{13}CO) maps has FWHM = $10.9'' \times 7.1''$ (FWHM = $11.5'' \times 8.7''$) and is oriented at P.A. = $73°$ (P.A. = $58°$). The noise (1 σ) in our ^{12}CO (^{13}CO) maps, as measured in channels with no signal, is 0.12 (0.08) Jy beam^{-1}. In our 3 mm continuum maps, σ = 4 mJy beam^{-1}. The conversion factor from ^{12}CO (^{13}CO) surface brightness to temperature units is 1.19 (1.01) K Jy^{-1} beam^{-1}. The coordinates of the tracking center in our maps are R.A. = $18^h 30^m 30.75^s$, decl. = $-14°28'56.28''$ (J2000.0).

3. OBSERVATIONAL RESULTS

3.1. Optical and NIR Imaging

The NIR and optical images of IRAS 18276−1431 are presented in Figures 1−4. IRAS 18276−1431 displays a clear bipolar morphology, with two lobes oriented along P.A. $\approx 17°-20°$ separated by a dark waist. Our AO images have higher angular resolution, probe deeper through the dusty nebula, have larger dynamical range, and provide more structural details than the *HST* images. In particular, they show a sharp drop of intensity at the lobe edges, which are quite well defined. The lobes also have limb-brightened tips (or "caps"), suggesting that they are closed-end structures. These caps are not visible in the optical images. The overall size and morphology of the two lobes are different, the southwest (SW) lobe being shorter and narrower than the northeast (NE) lobe. The morphological differences between the lobes are most prominent at the shortest wavelengths (optical and K_p-band images), where the SW lobe appears as a "two-finger" or ∧-like structure, in contrast to the more rounded NE lobe (Fig. 2, *right*).

The thickness of the dark equatorial waist between the lobes is larger in the optical images than in the NIR ones. This is because the optical depth of the material in the nebular equator obscuring the base of the lobes is expected to decrease with wavelength.
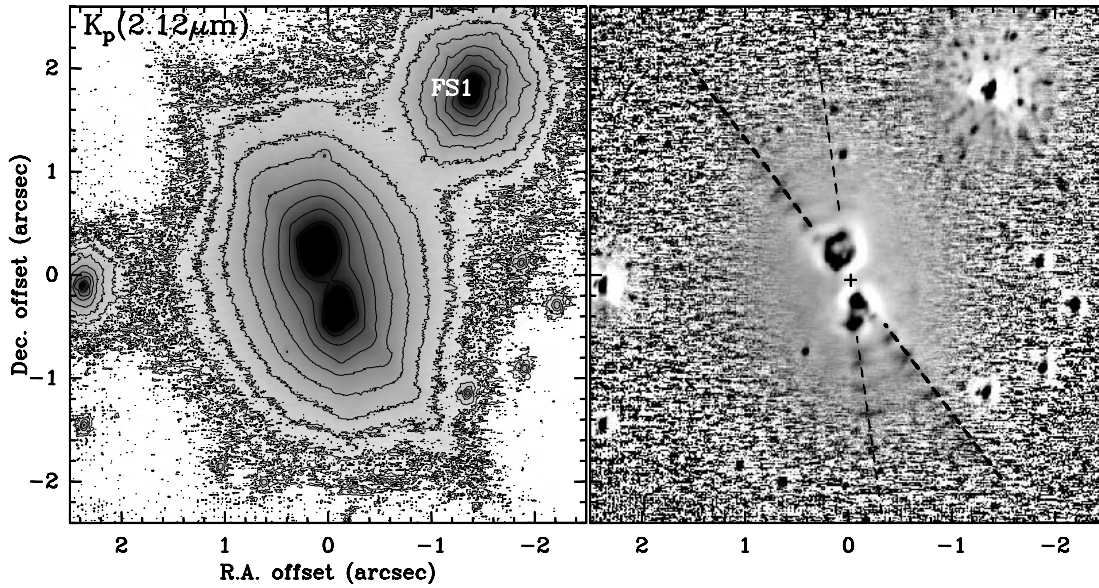
FIG. 2.—*Left*: K_p-band image of IRAS 18276−1431 showing the faint, elongated halo beyond the bipolar lobes. Intensity scale (shown in reverse gray scale) is the same as in Fig. 1. Contour levels are 3 $\sigma \times 2^i$ for $i = 0$−11 ($\sigma = 8 \times 10^{-6}$ mJy pixel^{-1}; Table 1). The two bright objects at offsets −1.4″, +1.8″ (FS1 in the text) and +2.4″, 0 are not physically associated with IRAS 18276−1431, as indicated by polarization maps of Gledhill (2005). *Right*: Sharpened version of the image on the left panel to show the searchlight beams and "arcs" of IRAS 18276−1431. The maximum (*black*) and minimum (*gray*) values of the displayed logarithmic intensity scale are set at 0.8 and 1.3, respectively. The cross indicates the point where the searchlight beams intersect each other. The center of the image (offset 0, 0) is the center of the halo (see text in § 3.1).

Radial cuts of the NIR intensity along the lobes (Fig. 5) show a central minimum, where the extinction reaches a maximum value, and two adjacent absolute maxima (or peaks) separated by a distance $2h = 0.34″$ in the L_p and M_s images. (In the K_p-band image the separation between the peaks is slightly larger presumably due to a larger optical depth in K_p.) The NIR optical depth along the line of sight at the peaks (i.e., at $\pm h$ from the central minimum) is expected to be $\ll 1$ given the sudden change in the slope of the radial profile (from a positive to a negative value): we start to see
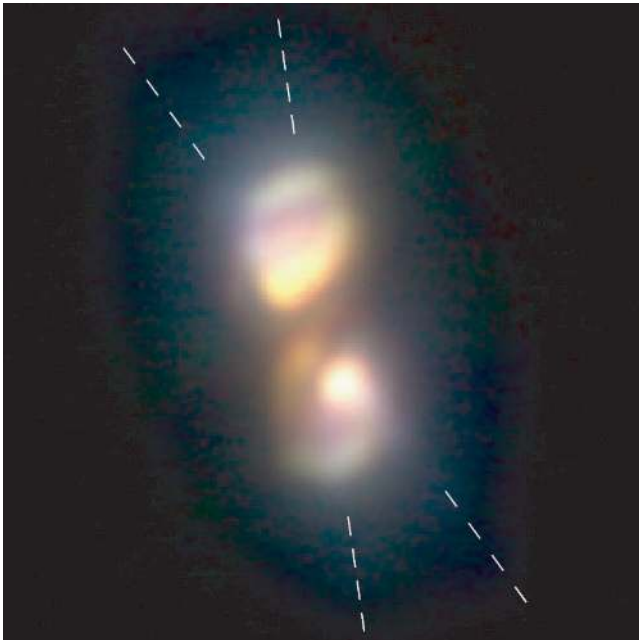

FIG. 3.—False three-color composite of the K_p (*blue*), L_p (*green*), and M_s (*red*) AO images in a square root intensity scale. Dashed lines indicate the orientation of the searchlight beams. Note the well-delineated lobe caps and the equatorial waist of dust obscuring the central star.

the base of the lobes through the waist. This probably indicates that the optical depth and, therefore, the column density of the waist decreases with latitude or, equivalently, with the distance above the equatorial plane. A density power law that decreases with the latitude is also inferred from modeling of polarimetric NIR data of IRAS 18276−1431 by Gledhill (2005).

Our deep NIR images also reveal a faint (sensitivity limited), elongated halo surrounding the lobes. The contribution of the extended PSF halo to this component is negligible, less than $\sim 1\%$−2%. The size of the halo is $4.5″ \times 3.4″$, as measured to a $\sim 3 \sigma$ level over the sky background in our K_p image, and decreases with increasing wavelength, suggesting that the halo consists of scattered starlight. The decrease of size with wavelength may also be partially due to the lower sensitivity in the L_p- and M_s-band images. The major axis of the halo is oriented along P.A. $\sim 17°$, similarly to the lobes, as seen in the optical and NIR images. (In contrast, the extended PSF halo, which is observed around bright field stars, is elongated toward the guide star.) In the L_p image, there is faint emission extended in the direction roughly perpendicular to the lobes, along P.A. $= 105°$−110°. The outer radius of this sensitivity-limited structure is 0.6″.

Our K_p image has revealed two pairs of radial "searchlight beams" emerging from the nebula center and directed oppositely through the nebular center along P.A. $\approx 36°$ and 8° (Fig. 2). The angular width of the beams in the azimuthal direction is ΔP.A. $\approx 15°$. The searchlight beams are not axially symmetric, the beams running along P.A. $= 36°$ being the brightest and the longest (observed up to $\pm 2.8″$ from the nebula center). The north searchlight beam directed along P.A. $= 8°$ is much fainter than its southern counterpart. The south beams seem to be the continuation of the inner and brighter $\wedge$-like feature observed in this lobe. There are several arclike features superimposed on the searchlight beams (see also Fig. 6). Some of these arcs are also observed with a much smaller brightness in the regions of the halo between the beams. The separation between the arcs is in the range 0.18″−0.24″, and some of them appear to intersect each other. The characteristic width of the arcs is $\lesssim 0.1″$.
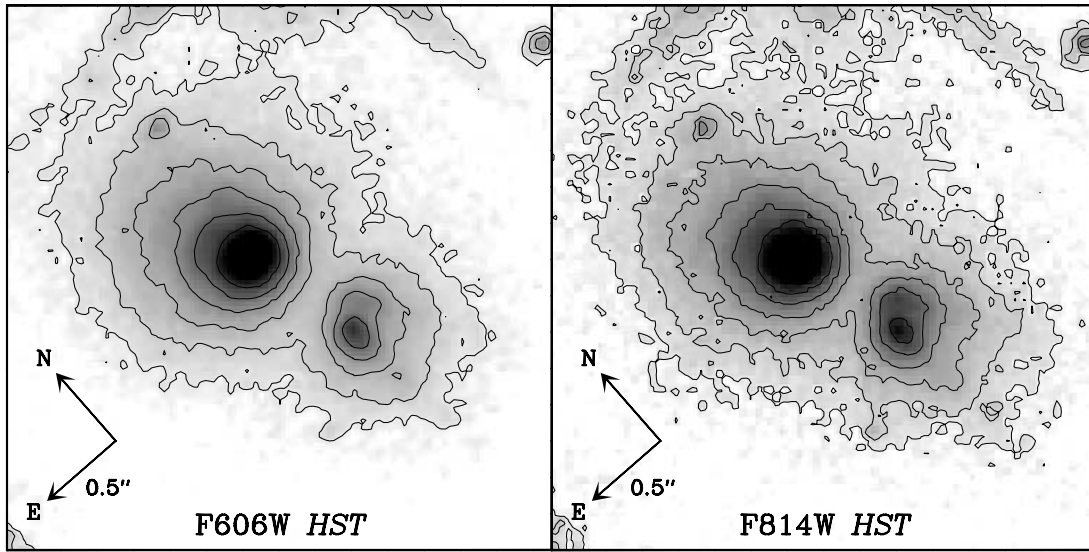
Fig. 4.—F606W and F814W WFPC2 *HST* images of IRAS 18276−1431 in a logarithmic intensity scale. Contour levels are 6 $\sigma \times 2^i$ for $i = 0-8$ (see Table 1 for values of σ). The north and east directions are indicated by the 0.5″ sized arrows.

The point where the beams cross at the nebula center (here-after beam center) does not coincide with the center of the halo (Fig. 2). The latter has been determined by fitting elliptical iso-photes[8] to the halo in K_p band: we have only used the isophotes with intermediate brightness, making sure that the main derived properties (center and shape) are not strongly affected by the bright-ness distribution of the lobes or bright field stars. The center of the beams has been estimated by taking azimuthal cuts with different center points along the polar axis. The center of the beams is defined to give the largest degree of symmetry in the width and position of the beams in the azimuthal cuts (we are assuming that the beams are intrinsically symmetric). The point where the beams cross at the nebula center and the center of the halo are separated by 53 mas along the direction of the lobes, which is larger than the expected errors in the location of the centers (errors <1 pixel ∼9 mas). Partial illumination of the halo by the light scattered in the lobes (in addition to the starlight) could explain the offset between the two centers and the similar orientation of the halo to that of the

---

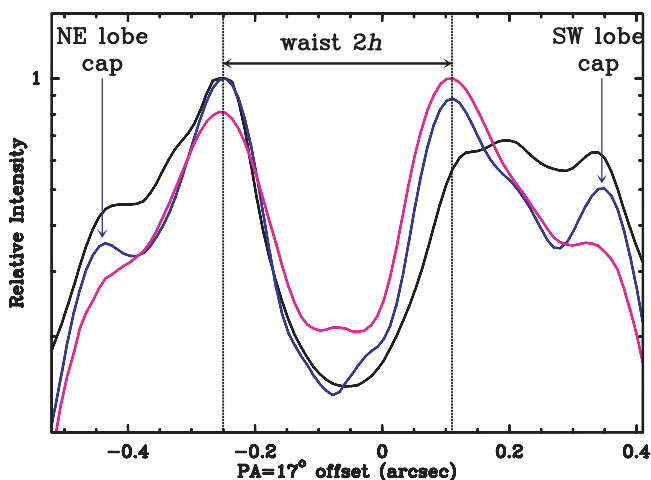[8] Using the IRAF task `stsdas.analysis.isophote.ellipse`.

Fig. 5.—Radial profile through the lobes along P.A. = 17° of the K_p (*black*), L_p (*blue*), and M_s (*pink*) images showing the dark waist and the lobe caps.

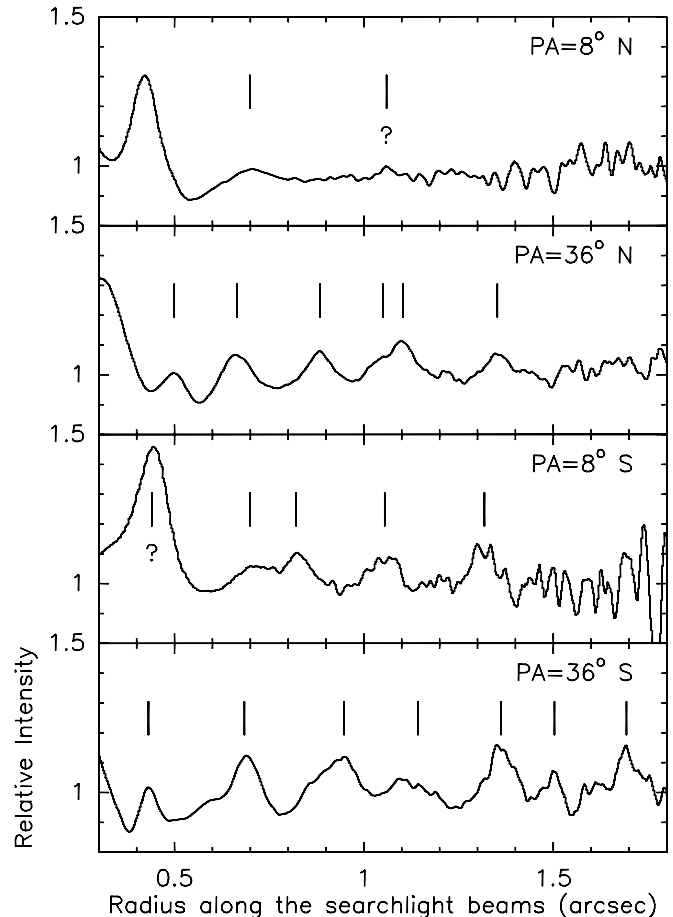
Fig. 6.—Radial profile of the K_p-sharpened image (Fig. 2, *right*) through the searchlight beams integrating azimuthally in the range P.A. = 6°−10° and 34°−38° showing the arcs (*vertical tick marks*). Question marks indicate tentative arcs.
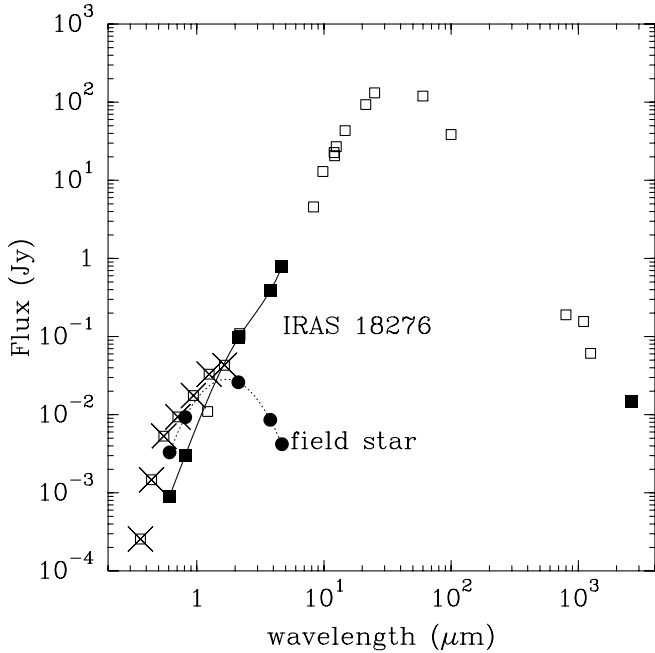
Fig. 7.—SED of IRAS 18276−1431 (*squares*) and the bright field star FS1 (*circles*; see Fig. 2). Data from this paper are plotted using filled symbols. Literature data points are represented by open squares (from the 2MASS and *IRAS* databases; Le Bertre 1987; van der Veen et al. 1995; Meixner et al. 1999). Crossed out symbols represent photometric data obtained with large apertures most likely including flux from FS1 and that overestimate the flux from IRAS 18276−1431. A solid (dashed) line has been used to delineate the SED of IRAS 18276−1431 (FS1) in the 0.6–3.8 μm range.

lobes: the center of the halo is expected to move in the direction of the brightest lobe, i.e., the NE lobe.

3.2. *Photometry*

The optical and NIR photometry (and other observational details) are given in Table 1. Total fluxes have been estimated by integrating the surface brightness of all pixels within a polygonal area enclosing the emission from our source with signal 3 σ above the sky and leaving outside bright field objects. Our fluxes in the visible are significantly smaller than those obtained from ground-based observations previously reported in the literature (see Fig. 7). This is because of the large apertures used in ground-based observations, which most likely included flux from the bright star FS1 northwest of IRAS 18276−1431 (Fig. 2). Our flux measurements in the NIR are also smaller than the 2MASS fluxes but are in excellent agreement with the *J* and *K* photometry by Gledhill (2005), obtained using an elliptical aperture including only flux from IRAS 18276−1431. The integrated flux in the NE lobe is larger than in the southeast (SE) lobe by a factor of 3–4 in the optical and 1.3–1.4 in the NIR (Table 1).

3.3. *Color Maps*

We have obtained color images of IRAS 18276−1431 (F814W−F606W, L_p-K_p, M_s-K_p, and M_s-L_p), which are shown in Figure 8. Registration of the *HST* optical and NIR images has been done using field stars to compute relative object shifts.[9] The estimated uncertainty in the image alignment is ∼1 pixel (i.e., ∼10 and ∼23 mas for the AO and *HST* images, respectively).

---

[9] Using the IRAF task images.immatch.imalign.

The reddest region in our F814W−F606W color map is not in the waist but in the base of the SW lobe, in a small region north of the relative maximum in the F814W and F606W surface brightness distribution. There is a color relative minimum at the waist, which is bluer than the base of both lobes.

In our higher resolution, better S/N NIR color maps, the nebular structure is much more clearly delineated. The L_p-K_p and M_s-K_p color images show an hourglass structure with an overall pointlike symmetry. The lobe walls and caps are quite well delineated in these images, in particular, in the L_p-K_p maps. The west (east) side of the north (south) lobe appears brighter. There is a relative color minimum (i.e., a relatively blue region) in the middle of the lobes, at a radial distance of 0.3″ from the center. As in the F814W−F606W color images, the L_p-K_p and M_s-K_p color images show a relative minimum in the waist. The elongation of the halo along P.A. = 105°−110° observed in the L_p-band images is also noticeable in the L_p-K_p image with relatively blue colors.

There are gradually increasing differences in the maps in going from L_p-K_p to M_s-K_p and to M_s-L_p: the lobe walls and caps smooth out, and the waist reddens (relative to the lobes). In the M_s-L_p map the color reddens gradually from the lobe tips to the waist, where the nebula is reddest. These trends are mainly the result of the lower scattering and absorption optical depths at these long wavelengths. The waist in the M_s-L_p image shows a similar orientation to the more extended equatorial structure seen in the L_p-K_p and L_p-band images.

3.4. *Millimeter-Wave Observations*

Unresolved ^{12}CO $J = 1−0$ emission is observed toward IRAS 18276−1431 within the LSR velocity range [+45 : +80] km s^{-1} (Figs. 9 and 10). The line profile is well fitted by a parabola centered at $V_{sys} = 62$ km s^{-1} (LSR) and total width (at zero intensity level) of 34 km s^{-1}. The parabolic profile is characteristic of unresolved optically thick CO emission and yields an expansion velocity of the molecular envelope of IRAS 18276−1431 of $V_{exp} = 17$ km s^{-1}. This value is comparable with, but slightly larger than, that derived from previous single-dish ^{12}CO $J = 2−1$ spectra and OH maser observations ($V_{exp} = 12–14$ km s^{-1}; Heske et al. 1990; Bowers et al. 1983). The observed ^{12}CO profile has a prominent, narrow absorption feature in the range [+64 : +69] km s^{-1} (LSR), i.e., blueward of V_{sys}, which is most likely due to interstellar absorption. For that reason, the integrated flux over the line profile is expected to be a lower limit to the intrinsic ^{12}CO flux from IRAS 18276−1431. A better estimate of the intrinsic flux from the source is given by the integral of the parabolic fit to the line profile, which we have used for the determination of the molecular mass in the envelope of IRAS 18276−1431 (Table 2 and § 7.2). The ^{12}CO emission integrated over the line profile is centered at R.A. = $18^h30^m30.67^s$, decl. = $−14°28'57.6''$ (J2000.0), with an error of ∼0.8″ both in right ascension and declination.

The ^{13}CO $J = 1−0$ emission is detected above a 2 σ level in channels [+53 : +58] km s^{-1} (LSR). Given its location, which coincides with the ^{12}CO and continuum source, the ^{13}CO line most likely arises in IRAS 18276−1431, but the observed profile is affected by strong interstellar absorption at LSR velocities [+64 : +69] km s^{-1} or even a broader velocity range, preventing us from obtaining an accurate characterization of the line profile. As for ^{12}CO, the measured ^{13}CO line flux is most likely a lower limit to the total flux emitted by IRAS 18276−1431. Parameters derived from our ^{12}CO and ^{13}CO maps are given in Table 2.

An unresolved, continuum source is detected toward IRAS 18276−1431 with a flux of $F_{2.6\,mm} = 15 \pm 4$ mJy. The contamination
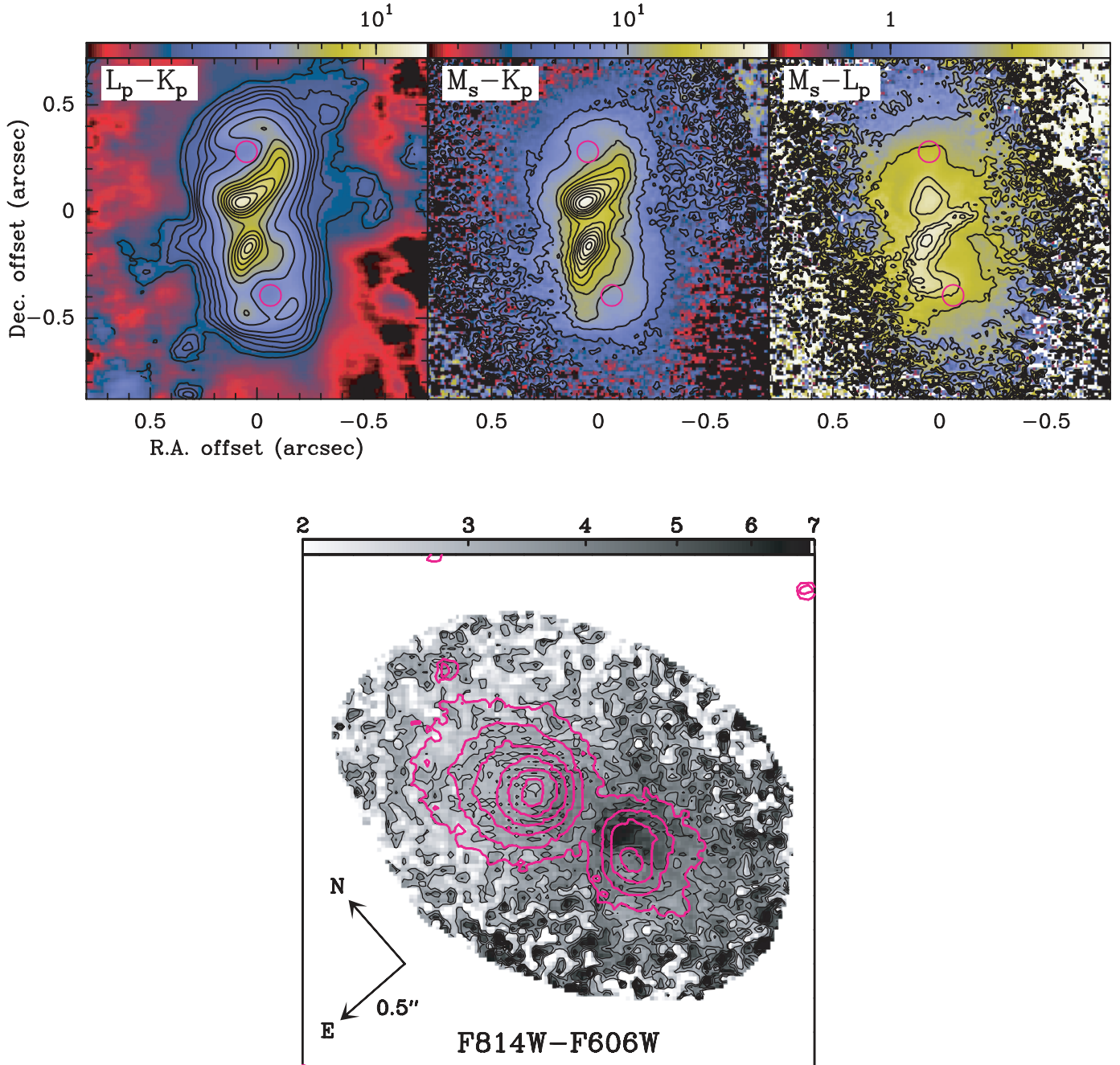
FIG. 8.—*Top*: Color maps obtained with the K_p, L_p, and M_s AO images. The color scale (in a logarithmic strecht) is shown in the wedge at the top of the boxes. Circles indicate the position and size of the small, relatively blue patches used for studying the central illuminating source (§ 5). *Bottom*: F814W−F606W color map (*gray scale*); the F814W image (*contours*) is superimposed.

of the continuum flux by ^{12}CO $J = 1-0$ line emission is less than 5%.

4. EXTINCTION TOWARD THE CENTRAL STAR

The extinction along the line of sight toward the central star in IRAS 18276−1431 must be quite high not only in the visible but also at the observed infrared wavelengths, since the illuminating star remains hidden even in the M_s band. We have estimated a lower limit to the optical depth (τ) at 2.12, 3.76, and 4.67 μm from the ratio between the observed surface brightness ($I_{\rm obs}$) and the expected unabsorbed intensity (I) per pixel from the central star. Adopting values for the stellar effective temperature and luminosity of $T_{\rm eff} = 7000$ K and $L = 6.4 \times 10^3$ $L_\odot$, a distance to IRAS 18276−1431 of $D = 3$ kpc (§ 1), and taking into account the PSF

in our images, we derive $I_{2.12\,\mu{\rm m}} = 4.3 \times 10^{-16}$, $I_{3.76\,\mu{\rm m}} = 9.9 \times 10^{-17}$, and $I_{4.67\,\mu{\rm m}} = 1.7 \times 10^{-17}$ ergs s^{-1} cm^{-2} Å^{-1} pixel^{-1}. The nondetection of the star at our 3 σ level (Table 1) implies that the total (circumstellar + interstellar) extinction toward the nebula center along the line of sight is $\tau_{2.12\,\mu{\rm m}} > 12.6$, $\tau_{3.76\,\mu{\rm m}} > 8.6$, and $\tau_{4.67\,\mu{\rm m}} > 5.4$. We have derived the interstellar extinction toward IRAS 18276−1431, $A_V = 1.6 \pm 0.5$ mag, using the numerical algorithm provided by Hakkila et al. (1997). For a standard total-to-selective absorption ratio $R_V = 3.1$, the above value of A_V yields the following estimates of the interstellar extinction: $A_{2.2\,\mu{\rm m}} = 0.3$ mag, $A_{3.76\,\mu{\rm m}} = 0.16$ mag, and $A_{4.67\,\mu{\rm m}} = 0.1$. Adopting these values, the *circumstellar* optical depth toward the star in IRAS 18276−1431 is $\tau_{2.12} > 12.3$, $\tau_{3.76} > 8.4$, and $\tau_{4.67} > 5.3$. These values are in agreement with the order of magnitude of the
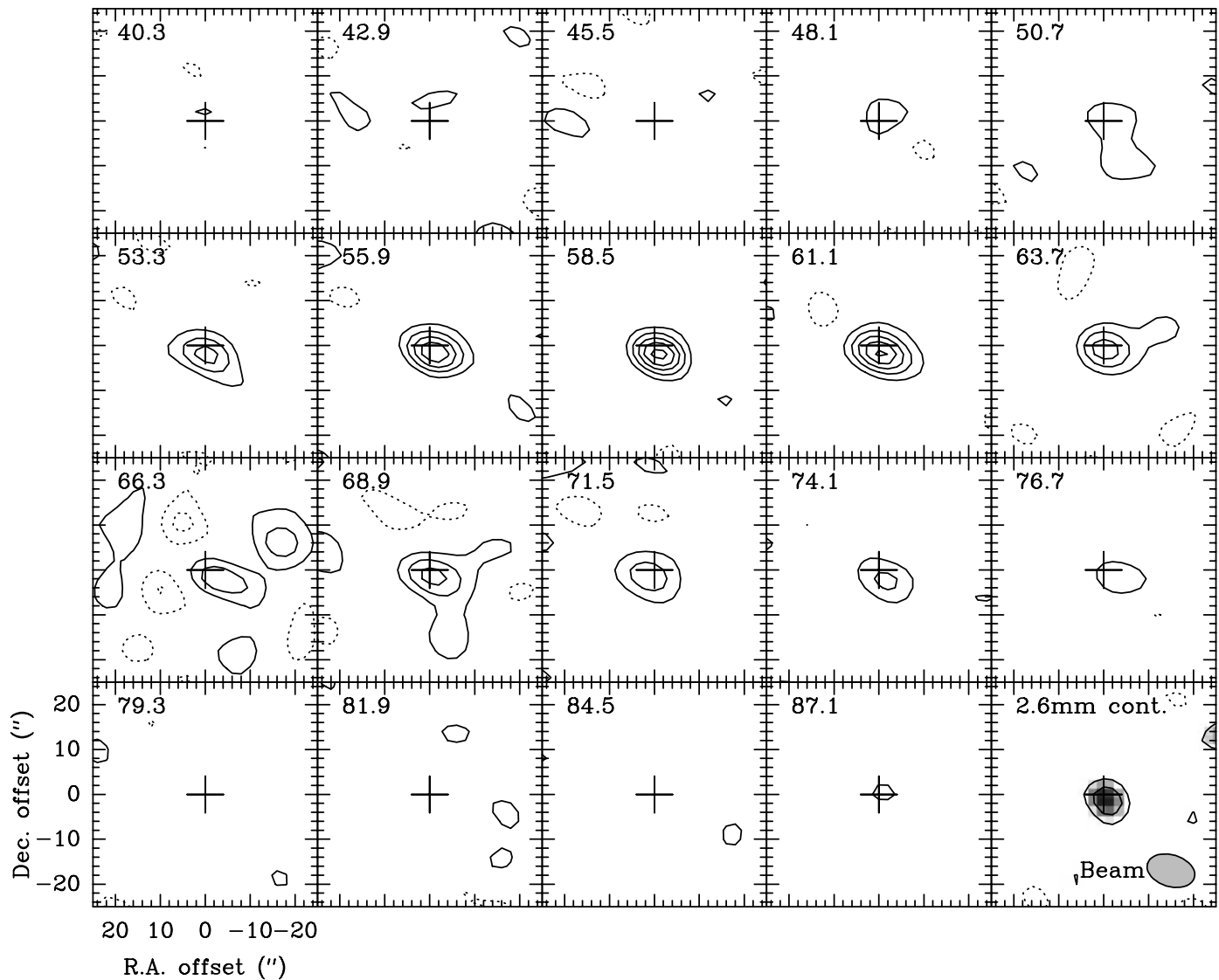
FIG. 9.—The ^{12}CO $J = 1-0$ velocity channel maps of IRAS 18276−1431 obtained with OVRO. The LSR velocities of the different channels are indicated in km s^{-1} units within the boxes. Levels are $-4, -2, 2, 4, \ldots, \sigma$ ($\sigma = 13$ Jy beam^{-1}). Positive (negative) contours are plotted using solid (dashed) lines. Brightness to temperature units conversion factor is 1.19 K Jy^{-1} beam^{-1}. The 2.6 mm continuum map and the clean beam, FWHM $\sim 10.9'' \times 7.1''$, are represented in the last panel. Levels of the continuum are $-2, 2,$ and $3\,\sigma$ ($\sigma = 4$ mJy beam^{-1}). The coordinates of the center of the maps (marked with a *cross*) are R.A. $= 18^{\mathrm{h}}30^{\mathrm{m}}30.75^{\mathrm{s}}$, decl. $= -14°28'56.28''$ (J2000.0).
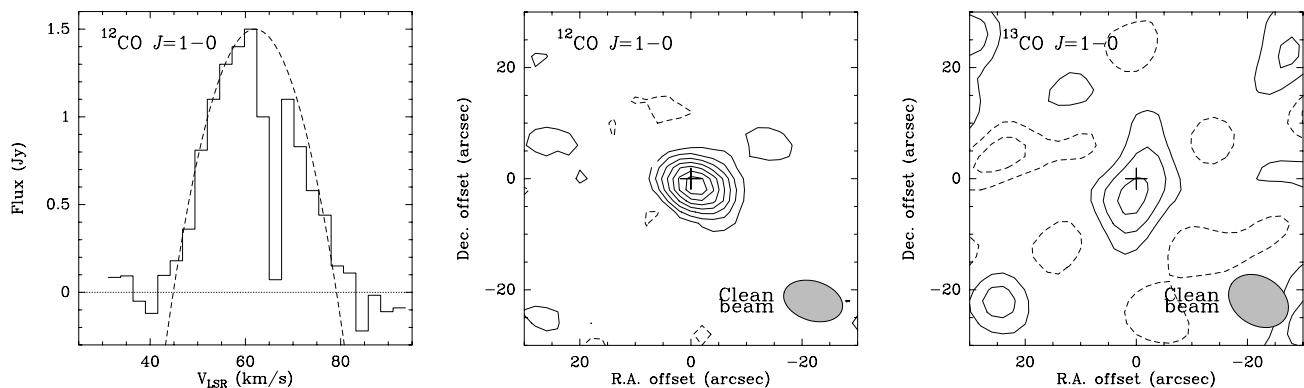

FIG. 10.—*Left*: ^{12}CO $J = 1-0$ spectrum integrated over the nebula (*solid line*) and parabolic fit to the ^{12}CO profile (*dashed line*). The ^{12}CO (*center*) and ^{13}CO (*right*) intensity maps are integrated over the line profile, i.e., within the LSR velocity range $\sim[40 : 80]$ and $[53 : 59]$ km s^{-1}, respectively. For ^{12}CO (^{13}CO) levels are $-2, 2, \ldots, \sigma$ spaced every $2\,\sigma = 3.4$ Jy km s^{-1} ($-2, -1, 1, \ldots, \sigma$ spaced every $1\,\sigma = 0.6$ Jy km s^{-1}).

TABLE 2
CO LINE PARAMETERS AND DERIVED MOLECULAR MASS

Parameter	^{12}CO $J = 1-0$	^{13}CO $J = 1-0$
V_{sys} (km s^{-1})	62	[a]
V_{exp} (km s^{-1})	17	[a]
I_{CO} (Jy beam^{-1})	1.5 ± 0.3	0.32 ± 0.08
$\int I_{CO}\, dV\, d\Omega$ (Jy km s^{-1}).....	27 ± 3 (34)[b]	$2^{c} \pm 1$
$X(CO/H_2)$.............................	2×10^{-4}	10^{-5}
T_{ex} (K)	110	110
M_{mol} ($M_\odot$)	>0.28 $(D/3$ kpc$)^2$	>0.38 $(D/3$ kpc$)^2$

[a] A reliable estimate of this parameter is not possible due to low S/N.
[b] Integrated flux of the parabolic fit to the ^{12}CO line profile (see Fig. 10 and § 3.4).
[c] Affected by strong interstellar absorption.

equatorial optical depth in the J band, $\tau_J \approx 10$, inferred from modeling of the polarimetric data (Gledhill 2005), and the mean optical depth in the 10–25 μm range, $\tau_{10-25\,\mu m} \gtrsim 1$, obtained from SED modeling (van der Veen et al. 1995; see also § 7.1), which indicates that the equatorial envelope around IRAS 18276−1431 is optically thick. Since the optical depth in the V band (0.55 μm) is typically a factor of ∼5 larger than in K band (2.12 μm) (for silicate dust $A_\lambda \propto \lambda^{-1}$; see § 7.1), the optical extinction toward the star must be $A_V > 60$ mag. This value is well above the lower limit to A_V derived directly from our *HST* F606W and F814W images following the procedure described above, $\tau_{0.606\,\mu m} > 15.4$ and $\tau_{0.814\,\mu m} > 14.1$.

5. THE ILLUMINATING SOURCE AT THE CORE OF IRAS 18276−1431

In this section we analyze the NIR colors of IRAS 18276−1431 and show that the lobes are illuminated partially by the starlight and partially by NIR light from a warm dust component, as has also been inferred for the bipolar PPN IRAS 16342−3814 (Sahai et al. 2005). The presence of warm dust around the central star of IRAS 18276−1431 is also deduced from the analysis of its full SED (Bedijn 1987 and § 7.1).

We analyze the observed NIR colors averaged over small apertures (of $\phi = 0.1''$) located in the middle of the lobes, where a relative minimum in L_p-K_p is observed. These regions (marked with circles in Fig. 8) are well removed from the lobe edges and the dense central waist, and therefore, the optical depths to scattered light are expected to be smallest. In the NW (SE) lobe we find that the interstellar extinction corrected intensities (I_ν) for 2.1, 3.8, and 4.7 μm are in the ratio 1:3.8:7.8 (1:3.7:8.5) indicative of a very red source illuminating the lobes (note that the two lobes give very similar colors). The observed colors in these regions result from a combination of reddening due to internal extinction, and blueing due to scattering, of light from the central illumination source. Although H$_2$ emission has been detected in IRAS 18276−1431, line emission is not expected to be a significant contribution to the emission in the NIR filters (K. T. E. Lowe et al. 2006, private communication—see also the featureless spectra of this object in the H, K, and L bands reported by Le Bertre et al. 1989). Therefore, the observed intensity of the scattered continuum in the reflection lobes (corrected for interstellar extinction as in § 4), I, is given by

$$I \sim I_0\, e^{-\tau}\left(1 - e^{-\tau_{los}^{sc}}\right), \qquad (1)$$

where I_0 is the emission from the central source, τ is the extinction (absorption + scattering) optical depth from the central source

to the scattering region and from the scattering region to the observer (i.e., radial + tangential), and τ_{los}^{sc} is the line-of-sight scattering optical depth at the observed region. The above expression is valid for scattering occurring predominantly in the lobe walls, which is a reasonable approximation for IRAS 18276−1431 (§ 6.1).

We have modeled the K_p-L_p and M_s-L_p colors (allowing ±20% errors) adopting the above formula and varying the temperature of the illuminating source. The absorption and scattering optical depths have been assumed to follow a power-law dependence with wavelength of the type $\sim\lambda^{-1}$ and $\sim\lambda^{-4}$, respectively, in the 2–5 μm range, as expected for silicate dust (e.g., Draine & Lee 1984; Suh 1999). We find that the NIR colors measured cannot be reproduced if the only illuminating source is the central star, which is expected to have an effective temperature in the range $T_{eff} = 4000-10,000$ K. To explain the NIR colors, a warm (300–500 K) dust component is needed. In particular, the best fit of the NIR colors is obtained if the nebula is illuminated partially by the central star (for which we adopted $T_{eff} = 7000$ K) and partially by dust at 400 K. Our best-fit model indicates that a significant fraction (∼80%) of the central star's light is absorbed by this warm dust cloud, which presumably covers a significant solid angle around the star. As shown in § 7.1 (Fig. 13), 400 K dust is expected to be located at $(7-9) \times 10^{14}$ cm (45–60 AU) from the central star. Our best-fit NIR color model also indicates that the light from both the star and the dust cloud is extinguished by $\tau_{2.12\,\mu m} \sim 3.7$ in its way to, and through, the lobes.

6. STRUCTURAL COMPONENTS IN IRAS 18276−1431

6.1. *The Bipolar Lobes*

Our NIR color maps and images suggest that the lobes of IRAS 18276−1431 are most likely cavities excavated in the AGB envelope (i.e., structures with dense walls and more tenuous interiors), the light from the central source being reflected by dust in the lobe walls. This is also believed to be the typical situation in many post-AGB nebulae, and in particular for IRAS 18276−1431, the OH maser spatiokinematic distribution suggests the presence of bipolar outflows carving out the polar regions of the envelope (§ 1). Our L_p-K_p color maps indicate that the lobes are wider than they appear in the K_p image and display a certain degree of point symmetry (see Fig. 11). Such a point symmetry indicates that the east and west walls of the lobes have different densities, with the west (east) wall of the NE (SW) lobe being the densest, and/or are illuminated differently from the central star. The searchlight beam oriented at P.A. $= 36°$ seems to go through the least dense lobe wall. The orientation of the lobes on the plane of the sky as measured in the NIR color maps (P.A. $\sim 15°$) is different than in the K_p image (P.A. $\sim 20°$). The polarization angle measured by Gledhill (2005), P.A. $= 23°$, is very similar to the average P.A. of the searchlight beams revealed by our AO images and is probably a better representation of the direction along which the bipolar cavities were excavated. The different orientation of the lobes in the color maps is most likely the result of large optical depth through the west and east sides of the NE and SW lobes, respectively. Although the north and south lobes appear quite different in the K_p image, they are similar in the color maps, suggesting that the real structure of the two lobes is not that different, and the ∧-like appearance of the SW lobe is mainly an illumination effect (presumably the same that produces the searchlight beams, which are similarly oriented).

Scattering structures will in general tend to smooth out in images at long wavelengths because the scattering efficiency decreases as λ^{-4}. This trend is observed in our images. The limb-brightened appearance of the lobe tips or caps in our NIR images, which are best seen in the L_p-band image, suggests that the scattering
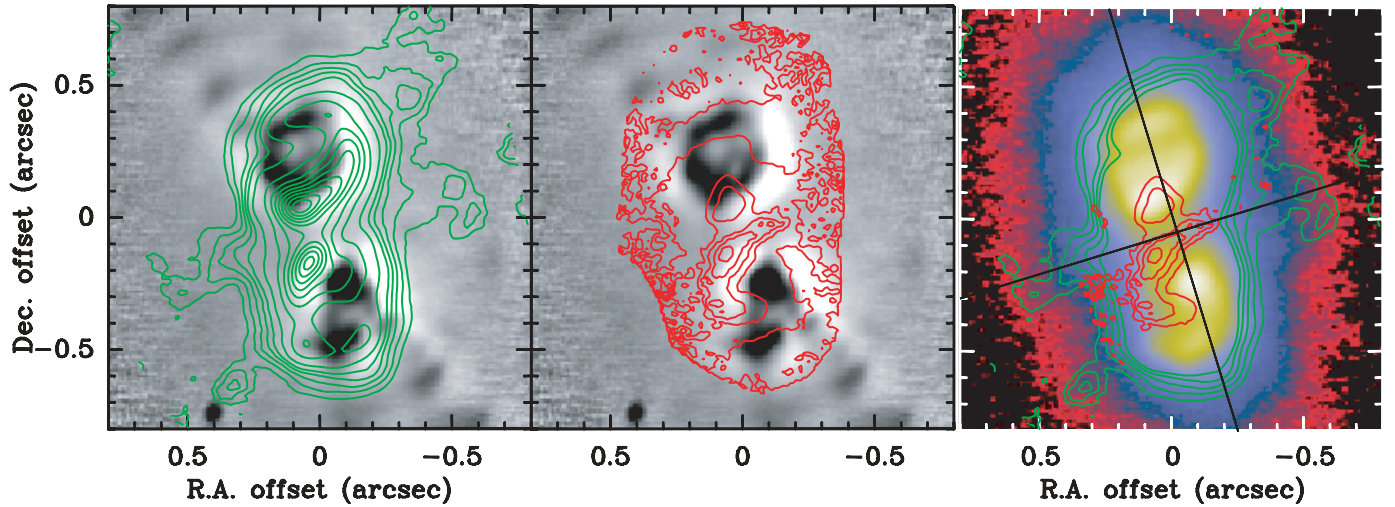
FIG. 11.—The L_p-K_p (*left*) and M_s-L_p (*center*) color maps (*contours*) superimposed on the sharpened K_p-band image (*gray scale*), and the L_p-band image (*right*). In the right panel only the lowest (highest) contours of the L_p-K_p (M_s-L_p) map are shown. The cross plotted is located at the point where the beams cross at the nebula center and is oriented along at P.A. = 17°. Note the similar orientation of the outer and inner equatorial structure probed by the L_p-K_p and M_s-L_p color maps, and the L_p-band images.

optical depth through these regions is <1. The caps are not observed in the optical images, which is consistent with the larger optical depths through the caps at shorter wavelengths. The structured lobe caps smooth out in the M_s image most likely because the radial and tangential scattering optical depth through the caps is too low at 4.67 μm: most of the light from the central source that reaches the inner edge of the caps escapes in the polar direction, and very little is scattered toward us. The radial cuts of the surface brightness along the lobes in the K_p and L_p images show that the caps move outward in going from K_p to L_p. The position of the lobe caps is very similar in the M_s and L_p images. This implies that the extinction in the polar direction through the caps at 2.12 μm is larger than 1. In the L_p band the lower extinction (<1) enables the photons to penetrate the lobe caps deeper. These values enable estimating a range for the optical depth through the lobe caps, $4 < \tau_V < 7$, adopting an extinction power law $\sim\lambda^{-1}$. This yields a range of $(2-4)\times10^7$ cm^{-3} for the mean density in the $\sim 0.1''$ wide caps, assuming a gas column density to optical extinction ratio of $N_d/A_V \sim 3\times10^{22}$ cm^{-2} mag^{-1}, which is expected for silicate grains and a dust-to-gas mass ratio of $\delta = 200$ (§ 7.1). Taking into account the size of the lobes and adopting a similar density throughout the lobe walls and caps, the total mass in the lobe walls must be $\gtrsim 10^{-2}$ $M_\odot$. The lower limit to the mass arises in the expected decrease of the density with the radial distance to the nebula center.

The redder F814W−F606W colors of the SW lobe can be interpreted as an indication that the SW lobe is the farthest of the two, the larger reddening being the combined result of (1) the presence of more dust in the halo and the extended equatorial disk lying in front of the distant lobe and (2) more efficient forward scattering (which would make the closer lobe appear brighter and bluer than the far one). The NE lobe is also the brightest in all the observed bands, which also favors its being the closest lobe. Note, however, that intrinsic differences in the dust density between the two lobes would affect their relative colors and brightness (e.g., Sánchez Contreras et al. 2004b).

6.2. *The Halo*

The halo of IRAS 18276−1431 most likely represents part of the CSE ejected during the AGB phase that has not been strongly affected by the lobe shaping processes. The halo is probably spher-

ical, the elongated shape being the result of the way the different regions of the halo are illuminated, in particular, of the lower optical depth along the poles and much larger extinction in the equatorial direction. The outer radius of the halo is $\gtrsim 2.8''$, as given by the length of the longest searchlight beams in the K_p band. The radial profile of the halo surface brightness (Fig. 12) can give us information about the spatial distribution of the density in the AGB envelope and how the mass-loss rate that led to this component might have varied in the past.

A cut of the K_p-band image along the nebular symmetry axis shows that beyond the tips of the lobes the halo radial profile varies with the radial distance to the nebula center like r^{-4}. A similar variation with r is observed in the L_p and M_s images. In the case of an optically thin scattering halo, the surface brightness varies proportionally to the light intensity dilution factor and to the line-of-sight scattering optical depth ($\tau_{\rm los}^{\rm sc}$) at each point. The light seen by the dust in the halo along the polar direction (P.A. = 20°) emanates mainly from the central source, which is expected to be pointlike. Therefore, the light intensity dilution factor will vary as $1/r^2$. After correcting the observed flux distribution by this factor, we deduce that $\tau_{\rm los}^{\rm sc} \propto r^{-2}$ in the halo. Since $\tau_{\rm los}^{\rm sc} \propto r^{1-\alpha}$ for a density power law $\propto r^{-\alpha}$, we conclude that $\alpha = 3$ in the halo. This result agrees with the dust density distribution $\propto r^{-2.6}$ deduced from SED modeling of IRAS 18276−1431 (van der Veen et al. 1995). The previous result is consistent with the AGB mass-loss rate increasing with time, assuming that the expansion velocity of the wind is time invariant.

The NIR surface brightness radial profile along the equator shows a r^{-3} dependence for radii larger than $0.6''$. This is consistent with the flux from these outer halo regions being mainly due to second- (or higher) order scattering. In fact, these equatorial regions are mainly illuminated by the two bright scattering lobes rather than by direct starlight, given the very large optical depth along the equatorial direction ($A_V > 60$ mag). In this case, the light intensity dilution factor is expected to have a dependence with r shallower than that for a pointlike illuminating source, probably of the type $1/r$, which is the dilution of a flux field emanating from an infinitely long wire (see Alcolea et al. 2001). After correcting by a $\sim 1/r$ dilution factor the observed flux distribution at radii $\gtrsim 0.6''$, we obtain $\tau_{\rm los} \propto r^{-2}$, which is consistent with a density law $\rho \propto r^{-3}$, as derived for the polar regions.
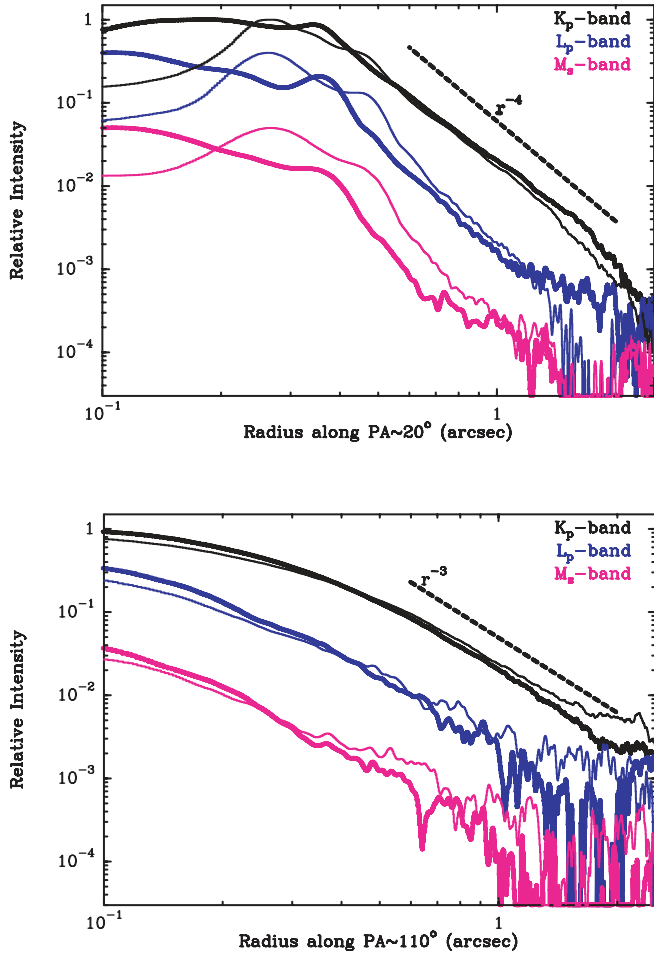
FIG. 12.—Surface brightness radial profiles through the center of the halo along the nebular major axis (P.A. = $15°-25°$; *top*) and the equator (P.A. = $105°-115°$; *bottom*) of the K_p (*black*), L_p (*blue*), and M_s (*pink*) images. Cuts are shifted by an arbitrary amount in the relative intensity axis for clarity. Thick (thin) lines are used for the NE (SW) lobe. Radial power laws $\propto r^{-4}$ and $\propto r^{-3}$ are shown for comparison (*dotted lines*).

The searchlight beams and arcs observed in the halo are most likely illuminated parts of the AGB shell viewed in scattered light. Discussion on the very uncertain origin of these features is deferred to § 8.

6.3. *The Waist*

The two lobes of IRAS 18276−1431 are separated by an equatorial dust waist/torus behind which the central star is hidden. OH maser emission is observed to arise in this equatorial torus over a range of angular radii of 0.25″ and 0.85″ (Bains et al. 2003; § 1). The spatial coincidence between the NIR dark waist and the OH maser emitting region is expected, since the OH masers are pumped by far-infrared (FIR) radiation from dust and are more likely to occur where the density is highest. The faint, equatorial structure seen in the L_p-band image with outer radius $R_{out} \sim 0.6″$ (§ 3.1) probably corresponds to outer parts of the equatorial torus, which are seen through multiply scattered light: a fraction of the photons scattered in the lobes are directed toward the equatorial plane and from there scattered again toward us. Although equatorial disks/tori are usually inferred from the presence of dark lanes separating the bipolar lobes, there are other PPNs in which these equatorial structures are observed in scattered light, e.g., IRAS 04296+3429 (Sahai 1999), IRAS 17106−3046 (Kwok et al. 2000), and IRAS 17347−3139 (Sánchez Contreras et al. 2006). The relatively

blue colors of the waist in the L_p-K_p and M_s-K_p color maps (§ 3.3) are consistent with multiple scattering illuminating with blue photons these equatorial regions, which otherwise would be expected to show the reddest colors. Since scattering is much less efficient at long wavelengths, the inner parts of the waist are best delineated in the M_s-L_p color map, where the waist displays the reddest colors, revealing the regions with the largest extinction along the line of sight.

As shown in § 4, the optical depth of the torus toward the central star along the line of sight is $A_V > 60$ mag. This value yields a column density of gas in front of the star of $N_d > 1.8 \times 10^{24}$ cm^{-2}, for a gas column density to optical extinction ratio of $N_d/A_V \sim 3 \times 10^{22}$ cm^{-2} mag^{-1} (see § 6.1). Adopting an outer radius for the torus of $R_{out} = 0.85″$, as given by OH maser emission mapping (see above), and assuming that the inner radius of the torus is much smaller than R_{out} (as indicated by SED modeling; § 7.1), the mean H$_2$ density in the torus toward the central star along the line of sight is $>5 \times 10^7 (D/3\ \mathrm{kpc})^{-1}$ cm^{-3}.

An order of magnitude for the total mass in the waist enclosed within a radius of $R \leq 0.85″$ and a height of $h \leq 0.17″$,[10] can be roughly estimated adopting a given density law as a function of the height above the equatorial plane, z. In the following, we consider two extreme cases for $\rho(z)$. For a constant density throughout the torus, $\rho(z) = $ constant, the total mass in this component would be $\gtrsim 4\ (D/3\ \mathrm{kpc})^2\ M_\odot$. A more realistic density law is one in which the density decreases with increasing z (§ 3.1). For example, for a steep exponential density law of the type $\rho(z) = \rho(0) \exp(-z \ln \chi/h)$, where $\chi = \rho(0)/\rho(h)$, the mass in the torus would be $\gtrsim 4 \times (1-1/\chi)/\ln \chi\ (D/3\ \mathrm{kpc})^2\ M_\odot$. Our NIR images suggest that the optical depth through the waist at h is probably <1 in the 2–4 μm wavelength range, since we start to see through the base of the lobes (§ 3.1). Since the extinction in the optical is typically a factor of 5 larger than in the K_p band, we estimate that $A_V(h) < 5$. Therefore, a reasonable lower limit to $\chi[\propto N_d(0)/N_d(h) \propto A_V(0)/A_V(h)]$ may be ≈ 10, which yields a total mass of $\approx 1\ (D/3\ \mathrm{kpc})^2\ M_\odot$. The mass derived is very uncertain, since the total extent of, and density distribution in, the torus as well as the geometry of the innermost nebular regions, which determines the way the nebula is illuminated, are unknown. Therefore, the above figure has to be taken only as an indication that the mass of this equatorial component could be quite large; in particular, it could represent a significant fraction of the total mass in the envelope. This is also observed in other post-AGB nebulae, for example, in OH 231.8+4.2, which has a dense ($\sim 3 \times 10^6$ cm^{-3}) equatorial waist that contains $\sim 70\%$ of the total envelope mass, as derived from high angular resolution CO mapping (Bujarrabal et al. 2002; Alcolea et al. 2001).

For a silicate + graphite mixture in the envelope of IRAS 18276−1431, which cannot be completely ruled out (see § 7.1), the density and the mass derived for the torus would be smaller. For example, the standard interstellar matter graphite and silicate mixture with a dust-to-gas mass ratio $\delta = 200$ yields $N_d/A_V \sim 1.5 \times 10^{21}$ cm^{-2} mag^{-1}. For this lower value of the N_d/A_V ratio, the mean density in the torus would be $\gtrsim 2 \times 10^6 (D/3\ \mathrm{kpc})^{-1}$ cm^{-3}, leading to a mass of $\sim (0.2-0.07)\ (D/3\ \mathrm{kpc})^2\ M_\odot$ for the two extreme (constant and exponential) density laws considered above.

7. MASS, MASS LOSS, AND DUST TEMPERATURE

7.1. *SED Modeling*

We have derived the physical parameters of the dust envelope of IRAS 18276−1431 by using a radiative transfer code to fit its

---

[10] Projection effects can be ignored, since the lobes are very close to the plane of the sky, and therefore, the torus is expected to be nearly edge-on (§ 1).

SED at wavelengths $\lambda \gtrsim 5$ μm, the region of the spectrum where dust thermal emission is the main contributor to the observed flux (Bedijn 1987). At $\lambda \lesssim 2$ μm the dominant contribution to the flux is the scattered light from the central source. In the range 2–5 μm, a combination of these two emission mechanisms is expected. Calculations were performed with the photoionization code CLOUDY (ver. 05.07) last described by Ferland et al. (1998). CLOUDY has a dust code built in that solves the time-independent radiative transfer equation under the constraint of radiative equilibrium. Details of the grain model are given in van Hoof et al. (2004). The code makes a comprehensive, detailed treatment of the grain physics that includes, e.g., quantum and stochastic heating, heating of the grains by Lyα photons, and the photoelectric effect. CLOUDY does not work under the optically thin approximation, but calculates the thermal dust continuum for optically thick envelopes.

We have assumed that the envelope is spherically symmetric. Despite the simplicity of this assumption, the code is expected to provide reasonable constraints to the mean properties of the dust envelope (mass and temperature). As shown by, e.g., Ueta & Meixner (2003), asymmetries in the density distribution would mostly affect the optical part of the SED but not the mid-IR/FIR, which is the spectral region we are modeling. Scattering is assumed to be negligible in our model. As discussed in detail by Bedijn (1987), this is a reasonable approximation at $\lambda \gtrsim 2$ μm for dust shells with intermediate optical depths (i.e., $\tau_{9.7\ \mu m} \sim 4$), which is the case for IRAS 18276−1431. Even for very optically thick envelopes, with $\tau_{9.7\ \mu m} \sim 30$, inclusion of scattering does not change significantly the SED in the wavelength range that we are modeling.

In order to calculate the SED of IRAS 18276−1431 we have adopted a series of input parameters. We have assumed that the central star has a blackbody spectrum with an effective temperature of $T_{\rm eff} = 7000$ K and bolometric luminosity of $L = 6400\ L_\odot$ (§ 1). We have adopted astronomical silicate grains, as suggested by the presence of a weak 9.7 μm silicate feature in the IR spectrum of IRAS 18276−1431 (Le Bertre et al. 1989; Bedijn 1987). The optical constants for astronomical silicates are from the calculations of Martin & Rouleau (1991), which extend the work of Draine & Lee (1984) to ionizing energies where the grains are strongly absorbing. The high-IR polarization measured in IRAS 18276−1431 suggests a population of small dust grains, with radii $a <$ 0.3 μm (Gledhill 2005). Therefore, we have used the grain size distribution adopted by these authors, that is, with minimum and maximum grain radii of $a_{\rm min} = 0.01$ and $a_{\rm max} = 0.3$ μm, and a power-law size index of -5.5. CLOUDY uses a spherical Mie code to generate the grain opacity as a function of wavelength for a given size distribution and grain material (van Hoof et al. 2004).

The other input parameters needed by the code to calculate the SED are the inner and outer radius of the envelope, and the density distribution. For the density, we have adopted a radial power law $\rho \propto r^{-\alpha}$ and a dust-to-gas mass ratio constant throughout the envelope with a value of $\delta = 200$, which is typical of post-AGB O-rich envelopes. As already suggested by Bedijn (1987), a two-shell structure with warm and cool dust is needed to reproduce the SED in IRAS 18276−1431. The inner, warm dust shell would represent a recent low mass-loss rate wind that started after the cessation of the heavy mass loss at the end of the AGB. The former period of heavy mass loss led to the outer, cooler envelope. In the outer shell, we have adopted $\alpha = 3$, as indicated by the radial profile of the halo in our NIR images. For the inner shell we have used $\alpha = 2$, which is expected for a time-invariant mass-loss rate at a constant expansion velocity. The free parameters of our model are the inner radius of the inner shell, $R_{\rm in,1}$; the inner

TABLE 3
Envelope Parameters from SED Modeling

Input Source Parameters	
$T_{\rm eff}$ (K)	7000
L ($L_\odot$)	6400
D (pc)	3000

Input Grain Parameters	
Composition	Astronomical silicates
$a_{\rm min}$ (μm)....................	0.01
$a_{\rm max}$ (μm)	0.3
$n(a)$............................	$\propto a^{-5.5}$
Gas-to-dust mass ratio	$\delta = 200$

Derived Parameters	
Inner shell:	
$\quad R_{\rm in,1}$ (cm)	6.3×10^{14}
$\quad R_{\rm out,1}$ (cm).............	1.6×10^{16}
$\quad T_{\rm dust}$ (K)	500–105
$\quad \rho(r)$	$\propto r^{-2}$
$\quad \dot{M}$ ($M_\odot$ yr^{-1})	3.2×10^{-5}
$\quad M$ ($M_\odot$)..................	0.007
Outer shell:	
$\quad R_{\rm in,2}$ (cm)	1.6×10^{16}
$\quad R_{\rm out,2}$ (cm).............	1.25×10^{17}
$\quad T_{\rm dust}$ (K)	105–50
$\quad \rho(r)$	$\propto r^{-3}$
$\quad \dot{M}$ ($M_\odot$ yr^{-1})	2.0×10^{-3}
$\quad M$ ($M_\odot$)..................	0.95
Large grain component:	
$\quad a$..............................	$\gtrsim 400$ μm
$\quad T_{\rm dust}$ (K)	150–20
$\quad M$ ($M_\odot$)..................	0.03–0.3

radius of the outer shell, $R_{\rm in,2}$ (which is also the outer radius of the inner shell); the outer radius of the outer shell, $R_{\rm out}$; and the density (or, equivalently, mass-loss rate for $V_{\rm exp} = 17$ km s^{-1}) at the inner radius of each shell. These parameters have been varied until a good match to the observations is obtained. The best-fit parameters have been determined calculating and minimizing a χ^2 function:

$$\chi^2 = (F_{\lambda,\rm obs} - F_\lambda)^2 / \sigma_\lambda^2, \qquad (2)$$

where σ_λ is the error of the observed flux $F_{\lambda,\rm obs}$, which has been assumed to be of 20% for all wavelengths in the range modeled (i.e., 5–100 μm).

The parameters describing the dust envelope for the best-fit model are given in Table 3. The resulting synthetic SED together with the radial dust temperature distribution are plotted in Figure 13. In this figure we also show the gas density distribution for the best-fit model for a constant gas-to-dust mass ratio throughout the envelope (see above) and the kinetic temperature of the molecular gas predicted by CLOUDY after solving the full physics (heating and cooling processes) for the derived envelope parameters.

The total mass in the envelope of IRAS 18276−1431 enclosed within an outer radius of $R_{\rm out} = 1.25 \times 10^{17}$ cm is ~ 0.95 $M_\odot$; most of it is in the outer, cooler shell. Larger values of $R_{\rm out}$ reproduce equally well the SED of IRAS 18276−1431; therefore, the value 0.95 $M_\odot$ may be a lower limit to the total mass. (For an outer radius of 10^{18} cm the total mass of the envelope would
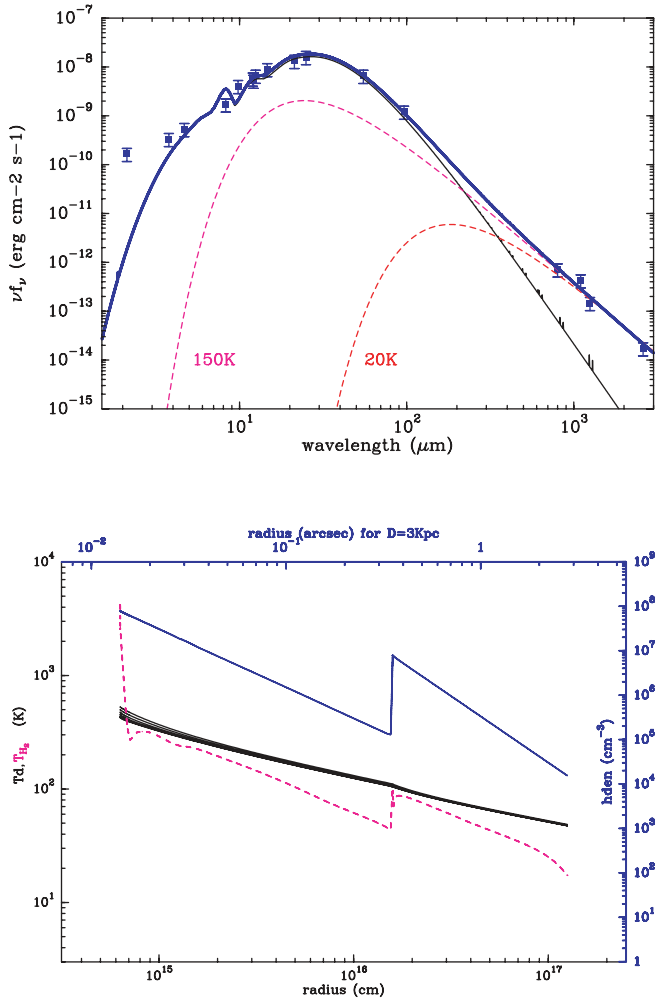
Fig. 13.—*Top*: Observed SED of IRAS 18276−1431 corrected by interstellar extinction (*squares*), SED predicted by CLOUDY for our best-fit model (*thin solid black line*), and blackbody spectra for $T_{dust} = 150$ and 20 K (*dashed lines*). A combined model spectrum (best-fit CLOUDY model + 150 K blackbody) is shown with the thick solid blue line. *Bottom*: Spatial variation of the grain equilibrium temperature for the different grain size bins used in the model (*solid black lines*). The gas density (*blue line*), obtained by adopting a constant dust-to-gas mass ratio throughout the envelope ($\delta = 200$), and the gas kinetic temperature (*pink dashed line*), predicted by CLOUDY for the best-fit envelope parameters derived from SED modeling, are also shown.

be 1.9 $M_\odot$.) Although the best-fit SED model is obtained for an inner radius of $R_{in,1} = 6.3 \times 10^{14}$ cm, values in the range $R_{in,1} = (5-8) \times 10^{14}$ cm lead to acceptable results. The optical depth is $A_V \sim 4$ mag, which is in good agreement with the optical depth of the 9.7 μm silicate feature derived by Bedijn (1987): note that the opacity of silicate grains as a function of wavelength is such that $A_V \sim \tau_{9.7\,\mu m}$. The extinction derived from SED modeling is much smaller than the extinction toward the central star along the line of sight (>60 mag) derived from our NIR images. This is expected, since SED modeling is done assuming spherical symmetry and, therefore, only provides *average* values for the envelope parameters. The relatively low value of A_V derived from SED modeling compared with $A_V > 60$ mag indicates a large equator-to-pole density contrast, consistent with the optical and NIR images. The dust temperature in the inner shell can be approximated by a radial power law of the type $T_{dust}(r) \propto r^{-0.4}$, except for the innermost regions where the temperature increases with a steeper slope. In the outer shell, the dust temperature decreases outward following a slightly shallower radial power law, $T_{dust}(r) \propto r^{-0.34}$. Average gas

densities in the inner and outer shell are in the range $\approx 10^5-10^8$ and $\approx 10^7-10^4$ cm^{-3}, respectively. Densities could be a factor of >15 larger in the equator and significantly smaller along the polar direction.

Our model clearly underestimates the observed fluxes in the submillimeter and millimeter wavelength ranges. Adopting a larger value for R_{out} has little effect on the flux at long wavelengths given the steep density law in the outer shell; therefore, a larger R_{out} cannot explain the emission excess. The emission excess could be partially accounted for by a dust emissivity function shallower than that assumed in our model, $Q_\lambda \propto \lambda^{-2}$, at wavelengths $\gtrsim 100$ μm. SED modeling of a number of AGB and post-AGB objects in the submillimeter and millimeter range suggest that the absorption efficiency of the dust in O-rich envelopes indeed follows a $\lambda^{-0.8}$ to λ^{-1} law (Knapp et al. 1993, 1994). However, from theoretical studies and laboratory works, an exponent ≤1.25 is only justified with difficulties (Gürtler et al. 1996 and references therein). The submillimeter and millimeter flux excess can also be explained if there is an additional component of larger grains, as has been inferred for a number of post-AGB objects (e.g., Walmsley et al. 1991; Jura et al. 1997; Sánchez Contreras et al. 1998; Sahai et al. 2006). The SED of IRAS 18276−1431 in the 800 μm–2.6 mm range is very well fitted by that of a blackbody in the Rayleigh-Jeans (R-J) limit, i.e., $f_\nu \propto \nu^2$ (Fig. 13). Since grains are expected to radiate like blackbodies at wavelengths $\lambda < 2\pi a$, an additional population of grains with radii $a \gtrsim 400$ μm would explain the observed spectral index of the continuum at long wavelengths. The temperature of this large grain component must be in the range $\sim 150-20$ K: if $T_{dust} > 150$ K, then we would obtain too much flux at $\lambda \lesssim 100$ μm; also T_{dust} must be $\gtrsim 20$ K, since the spectral index in the 800 μm–2.6 mm is consistent with blackbody emission in the R-J limit. Since the dust model built in CLOUDY does not allow in its current version grains larger than 5 μm, we have estimated the mass of large grains needed to account for the millimeter continuum flux, as explained in Sánchez Contreras et al. (1998). We have adopted a mean grain density and radius of $\rho = 3$ g cm^{-3} and $a \gtrsim 400$ μm, respectively. Assuming that the dust emissivity at $\lambda < 2.6$ mm is $Q_\lambda \sim 1$, we estimate that a total mass of dust of $M_{dust} \gtrsim 1.6 \times 10^{-4}$ $(D/3$ kpc$)^2$ $M_\odot$, for $T_{dust} = 150$ K, and $M_{dust} \gtrsim 1.6 \times 10^{-3}$ $(D/3$ kpc$)^2$ $M_\odot$, for $T_{dust} = 20$ K, is contained in this big grain dust population. Adopting a gas-to-dust mass ratio of $\delta = 200$,[11] the total gas mass associated with this large grain component is $M \sim (0.03-0.3)$ $(D/3$ kpc$)^2$ $(\delta/200)$ $M_\odot$. The location of this large grain component is unknown, since the millimeter continuum emission is unresolved in our $\sim 8''$ resolution maps. Cold (20–30 K), big grains have been inferred to be located in the dusty equatorial regions of some PPNs, where the grains are shielded against the starlight due to the large extinction along the equator (e.g., IRAS 22036+5306; Sahai et al. 2006). The temperature of the large dust component in IRAS 18276−1431 is not well constrained, and therefore, there is not a sufficiently strong reason to claim that the grains are in the dark (cold) waist. Big grains are also believed to grow in long-lived, orbiting disks (e.g., Red Rectangle; Jura et al. 1997). High angular resolution mapping of the submillimeter or millimeter continuum emission and/or measurements of the continuum in the $\lambda \sim 300-500$ μm range are needed to unveil the location of the big grains in IRAS 18276−1431.

Finally, our model predicts a 9.7 μm silicate feature that is slightly stronger than observed; however, we have not found any models that simultaneously produce a weaker silicate feature

---

[11] In the absence of reliable estimates of δ for the large grain component in CSEs, we adopt the same value as for the "normal" dust component.

and provide a good fit of the SED. This may suggest that there is a certain mixture of grains with different composition in IRAS 18276−1431.

7.2. The Mass from CO Data

As for most PPNs, the CO emission most likely arises in an expanding envelope that is the remnant of the AGB envelope and that is probably the counterpart to the NIR halo and waist. We have estimated the mass of this component from the ^{13}CO and ^{12}CO $J = 1-0$ flux. We have assumed that both lines are thermalized, i.e., the CO excitation is described by a rotational temperature that is similar to the kinetic temperature, T_{kin}. The thermalization assumption is a reasonable approximation for most PPNs and, in particular, is expected to be valid for IRAS 18276−1431, which has nebular densities larger than the CO $J = 1-0$ critical density ($\approx 10^3$ cm^{-3}) in most regions of the CO-emitting envelope probed by our maps ($R_{CO} < 5''$), as shown in Figure 13. We have used the mean kinetic temperature of H$_2$ predicted by CLOUDY for our best-fit model (Fig. 13) to estimate the molecular mass from CO. We have adopted a mean temperature of $T_{kin} = 110$ K and a relative ^{12}CO to H$_2$ abundance of 2×10^{-4}, and ^{13}CO to H$_2$ abundance of 10^{-5}, which are common values in PPNs (Bujarrabal et al. 1997, 2001, and references therein), and the well-known molecular parameters of CO (partition function, Einstein coefficients, etc.; see, e.g., Rohlfs & Wilson 2000). We derive a total mass of molecular gas in IRAS 18276−1431 of >0.28 $M_\odot$ from ^{12}CO (using the integrated flux of the parabolic fit to the line profile) and >0.38 $M_\odot$ from ^{13}CO (Table 2). The lower limit to the mass derived from ^{12}CO is because this line is optically thick, as indicated by its parabolic profile. Additional confirmation is given by the intensity ratio between the ^{12}CO $J = 2-1$ line, which was observed by Heske et al. (1990) with the IRAM 30 m radio telescope (beam = $21''$) with a main-beam temperature of $T_{mb} = 1$ K, and the $J = 1-0$ line, for which we measure $T_{mb} = 1.8$ K with a $10.9'' \times 7.1''$ beam. This yields a beam-corrected $J = 2-1$ to $J = 1-0$ line ratio of ~ 1, which indicates that both lines are optically thick through most regions of the CO-emitting envelope. The lower limit to the mass derived from the ^{13}CO line arises because of the strong interstellar absorption of the circumstellar emission and maybe because of a large optical depth in this transition as well. The fact that the mass derived from ^{12}CO is smaller than that derived from ^{13}CO, which is expected to be less opaque, is in agreement with the ^{12}CO $J = 1-0$ transition being optically thick.

The lower limit to the mass derived from CO is in agreement with the total mass obtained from SED modeling, ~ 1 $M_\odot$. The total mass enclosed within the upper limit to the outer radius of the CO-emitting nebula probed by our maps, i.e., within $5''$ (2×10^{17} cm), is 1.2 $M_\odot$, which is also consistent with the lower limit to the mass obtained from CO.

We note that values of T_{kin} of order $\approx 10^2$ K are expected and observed in young PPNs with dense envelopes (e.g., CRL 618; Sánchez Contreras et al. 2004a; see also Hrivnak & Bieging 2005). Values of T_{kin} as low as 15–30 K are also observed, however, in a number of PPNs (Bujarrabal et al. 2001). For a mean value of the kinetic temperature of 50 K, which is the average of T_{kin} over volume for IRAS 18276−1431 (Fig. 13), the lower limit to the mass derived from ^{13}CO is ~ 0.2 $M_\odot$.

8. FORMATION AND EVOLUTION OF IRAS 18276−1431

The analysis of our high angular resolution NIR and optical images, and the SED of IRAS 18276−1431, enable us to trace back in time the evolution of this object and to attempt to understand how the different structural components revealed by our data

were formed. From the values for the outer and inner radius of the outer dust shell of IRAS 18276−1431 ($R_{out} \gtrsim 1.25 \times 10^{17}$ and $R_{in,2} = 1.6 \times 10^{16}$ cm; Table 3) and the expansion velocity derived from CO, $V_{exp} = 17$ km s^{-1}, we infer that the heavy mass-loss process that led to this component started at least ~ 2300 yr ago and ceased ~ 300 yr ago. During that time the mass-loss rate increased from $\dot{M} \sim 2 \times 10^{-4}$ to 2×10^{-3} $M_\odot$ yr^{-1}. This heavy, time-increasing mass-loss rate wind, which is expected at the end of the AGB phase, was succeeded in IRAS 18276−1431 by a lower mass-loss rate wind ($\dot{M} \sim 3 \times 10^{-5}$ $M_\odot$ yr^{-1}), which could have stopped or been replaced with an even more tenuous wind recently (≈ 10–15 yr ago). The presence of bipolar lobes in IRAS 18276−1431 may imply large expansion velocities in some regions of the envelope (mainly along the polar axis). Although most of the dust is expected to be located in the massive AGB envelope, some dust fraction is located in shock-accelerated regions (e.g., the lobe walls), which are expected to have a complex and unknown kinematics. Therefore, the ages derived above assuming $V_{exp} = 17$ km s^{-1} are uncertain, especially for the inner dust shell.

As proposed for most PPNs (§ 1), the lobes of IRAS 18276−1431 have probably been excavated by interaction of fast, bipolar (jetlike) winds with the AGB envelope. The jet-launching mechanisms, which are believed to operate in the early post-AGB or late AGB phase, are still the subject of a vigorous debate. From the deprojected total length of the lobes ($0.5'' \sim 2.2 \times 10^{16}$ cm) and adopting an expansion velocity of ≈ 100 km s^{-1}, which is typical of bipolar post-AGB outflows (e.g., Bujarrabal et al. 2001), we estimate a value of ~ 65 yr for the kinematic age of the lobes. As shown by our NIR color maps, the lobes display a certain degree of point symmetry. Such a symmetry is found in many post-AGB objects and is often interpreted as a signature of precessing jetlike winds (e.g., Sahai et al. 2005).

The origin of the equatorial waist/torus is very uncertain. Given the large extent of the torus compared to the bipolar lobes, we believe that the waist is unlikely the result from the interaction of fast jets with an initially isotropic AGB wind. If the waist is just what is left of the AGB CSE after the jet + "AGB envelope" interaction, then we should observe a spherical envelope with a central biconical cavity that is as large as the optical lobes. In contrast, the dense material in the waist obscuring the central star and the base of the lobes is constrained to the equatorial region, forming a torus that extends up to a radius of $\gtrsim 0.6''$ ($\gtrsim 2.7 \times 10^{16}$ cm), as derived from our L_p-band images, and maybe of $\gtrsim 0.85''$ ($\gtrsim 3.7 \times 10^{16}$ cm), as derived from OH maser emission mapping (§ 1). It may be possible for shocks developed in the jet + AGB envelope interaction to move sideways and backward, compressing the gas in the equatorial plane and shaping the torus. However, since these shocks are expected to be much weaker and slower than the forward shocks that produce the lobes, they can form, at best, a torus whose radius is much smaller than the length of the lobes, contrary to what we observe. Alternatively, the waist of IRAS 18276−1431 could be the result of a period of enhanced mass loss concentrated in the equatorial plane. However, what induces such a heavy and asymmetrical mass loss is unknown, especially considering that the mass in the disk, although very poorly determined, could be a significant fraction of the total mass in the envelope (§ 6.3). Adopting an expansion velocity of $V_{exp} = 17$ km s^{-1}, we estimate that the kinematic age of the torus is $\gtrsim 700$ yr.

Searchlight beams and arcs like those observed in IRAS 18276−1431 are two of the most fascinating, yet poorly understood features revealed by recent high angular resolution, high-sensitivity images of AGB and post-AGB objects. Beams and arcs are most likely

illuminated portions of the envelope viewed in scattered light. As proposed by Sahai et al. (1998), searchlight beams may result from starlight escaping through holes/cavities in an inner dust cocoon. The agent excavating the holes is unknown, but it may be the same collimated (precessing) jets responsible for carving out the bipolar lobes. Morris (1981) had originally proposed another, more simple, scenario to explain the structure of bipolar reflection nebulae including searchlight beams, which were observed as small protrusions on the reflection lobes of some PPNs in *low angular resolution* images. In this scenario, which was also adopted in the scattering models by, e.g., Yusef-Zadeh et al. (1984) and Latter et al. (1993), these protrusions result from a density law that declines with latitude above the equatorial plane if, at some latitude, the radial optical depth to starlight falls rapidly below unity. As extensively discussed by Sahai et al. (1998), the latitude-dependent density model, however, was not able to explain satisfactorily the detailed morphology of the searchlight beams in the PPN CRL 2688 as observed with *high angular resolution*. Some of the objections to such a model argued by Sahai et al. (1998) also apply to IRAS 18276−1431. In particular, our images do not show any evidence of systematic ellipticity in the arcs, as would be expected in Morris's scenario. Moreover, the latitude-dependent density scenario does not account for the sharp edges and relatively large width of the searchlight beams in IRAS 18276−1431 (ΔP.A. $\approx 15°$; § 3.1). Nor does it account for the point symmetry of the searchlight beams, as observed in our K_p-band image (§ 3.1), which would require a point-symmetric density distribution at a spatial scale as large as the extended halo, where the beams are observed up to a radial distance of $\pm 2.8''$. Such a density law would be very difficulty to support, since it would imply a point-symmetric mass loss during the AGB phase. As far as we know, searchlight beams are also observed in the PPNs: CRL 2688 (Sahai et al. 1998), IRAS 20028+3910 (Hrivnak et al. 2001), IRAS 17150−3224 (Su et al. 2003), and IRAS 17245−3951 (Hrivnak et al. 1999), raising to five the number of PPNs with searchlight beams. The increasing number of objects with beams suggest that these are not extremely rare features, and therefore, the dust distribution required to explain the beams must be relatively common at least during some time in the evolution of these objects. It is worth noting that the five objects listed above display bipolar morphology, have dense, equatorial waists, and are seen nearly edge-on (IRAS 20028+3910 appears to be at an intermediate orientation; Su et al. 2001). The presence of a nearly edge-on, dark waist may then be a necessary condition for the observation of the beams. This is in part expected because scattering features will be necessarily more difficult to observe in objects with very bright cores outshining the nebula. Another interesting aspect is that beams are not observed in PNs or AGB envelopes, but only in young PPNs. The lack of beams in PNs may be an observational effect, since their bright central stars are usually directly visible and the scattering nebula is very diluted. The lack of beams in AGB envelopes is consistent with the idea that the winds clearing out the holes in the cocoon start after the star has left the AGB. The spectral types of the searchlight beam's PPNs are concentrated in the F–G range. This may be partially due to destruction of the dust cocoon by the high-velocity outflow responsible for carving out the holes and/or by the increasing stellar UV field as the star evolves toward hotter spectral types. Finally, the presence/absence of searchlight beams does not seem to be strongly correlated with the chemistry, since beams are observed both in C- and O-rich objects; however, a larger sample of searchlight beam PPNs is needed to reach reliable conclusions.

Arcs and rings are also getting more and more common in PPNs. Up-to-date arcs have been detected in seven PPNs (including IRAS
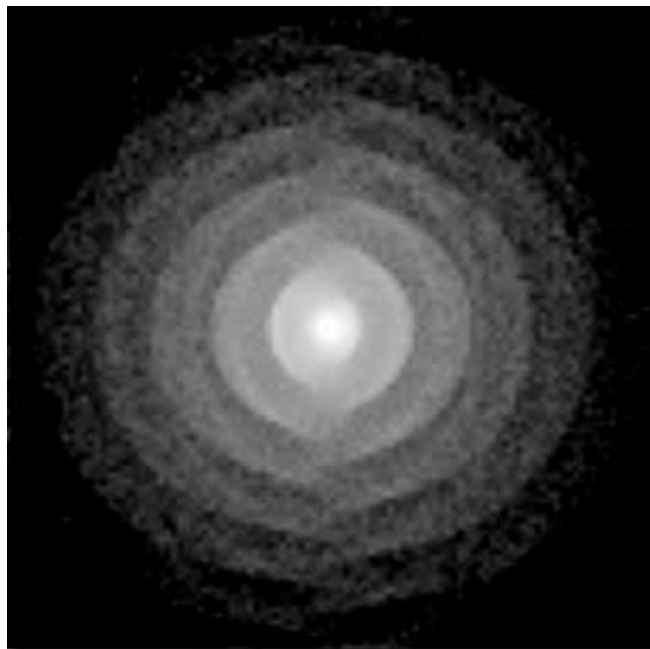

Fig. 14.—Model of spiral density shells induced in a circumstellar outflow by orbital motion in a binary system. The gray scale shows the projected dust density for an observer lying in the system's orbital plane—projected as a horizontal line running through the center. (The projection from most other angles has a spiral form.) To compare with the observations of IRAS 18276−1431, the dust distribution should be convolved with the illumination pattern, which is strongest along a cone centered on the system's angular momentum axis—projected as a vertical line through the center. The details of this model are described separately (M. Morris et al. 2007, in preparation).

18276−1431), four PNs, and one AGB envelope (see summary of arcs/rings in post-AGB objects by Su [2004]). The binary-induced spiral outflow model originally proposed by Mastrodemo & Morris (1999) produces arclike features very similar to those observed in IRAS 18276−1431 for a system viewed from near the equatorial plane and taking into account illumination effects (such as very large extinction along the equator by the dusty waist). In this model (see Fig. 14), the arcs disappear along the polar axis and alternate in radius on each side of the bipolar axis. The alternating arcs spaced along the polar axis are best seen if the angular momentum axis of the system is perpendicular to the line of sight. From our point of view, the most attractive aspect of the binary-induced spiral outflow model is the ability to explain the non-concentric, intersecting arcs of IRAS 18276−1431. This model has also been proved to explain the spiral pattern recently discovered in the extended envelope of the PN AFGL 3068 (Mauron & Huggins 2006; M. Morris et al. 2007, in preparation). A possible argument against this model is that it predicts arcs separated at quite regular intervals, set by the orbital period, whereas the time spacing of the arcs in IRAS 18276−1431 ranges between 190 and 250 yr for $V_{\rm exp} = 17$ km s^{-1}. Models involving magnetic activity cycles (e.g., Soker 2000; García-Segura et al. 2001) appear as an interesting alternative possibility to explain non-regularly spaced arcs. However, it is not known whether or not magnetic periodic variations can happen on a scale of hundreds of years, as required to explain the arc spacing in most PPNs (Su 2004).

9. SUMMARY

We present and analyze NGS-AO images in the K_p, L_p, and M_s filters of the PPN IRAS 18276−1431 obtained with the Keck II

10 m telescope. Supporting optical F606W and F814W *HST* images as well as interferometric observations of the ^{12}CO $J = 1$–0, ^{13}CO $J = 1$–0, and 2.6 mm continuum emission with OVRO are also presented. Our main findings are summarized as follows.

1. Our AO images reveal the structure of the dust envelope around IRAS 18276−1431 with $0.06''$–$0.1''$ resolution. The envelope of IRAS 18276−1431 displays a clear bipolar morphology with two lobes separated by a dark waist and surrounded by a faint, sensitivity-limited halo. Our K_p-band image reveals two pairs of radial "searchlight beams" emerging from the nebula center and several intersecting, arclike features.

2. The lobes are probably cavities with dense walls and caps excavated in the AGB envelope presumably by tenuous bipolar winds. The point symmetry displayed by the nebula may suggest that these bipolar winds are precessing. Although quite uncertain, our estimate of the total mass in the lobe walls is $\gtrsim 10^{-2}\ M_\odot$. For an adopted lobe expansion velocity of 100 km s^{-1}, which is typical of post-AGB outflows, we estimate a kinematic age $\sim$65 yr for this component.

3. The halo most likely represents the remnant of the AGB CSE that has not been strongly affected by the process that produces and shapes the lobes. The density in the NIR halo follows a radial power law $\propto r^{-3}$, which is consistent with a mass-loss rate increasing with time during the latest stages of the AGB. The outer radius of the halo is $\geq 1.25 \times 10^{17}$ cm, which implies that the halo was ejected $\gtrsim$2300 yr ago, for an expansion velocity of $V_{\rm exp} = 17$ km s^{-1} (see below).

4. The illuminating star remains hidden behind the dark waist even in the M_s-band images. Such a waist most likely represents a dense equatorial torus, also traced by OH maser emission, that could have resulted from equatorially enhanced mass loss. The *circumstellar* optical depth toward the star along the line of sight (i.e., through the torus) derived from our NIR images is $\tau_{2.12} > 12.3$, $\tau_{3.76} > 8.4$, and $\tau_{4.67} > 5.3$, which implies a large extinction in the optical, $A_V > 60$ mag, and a mean density $>5 \times 10^7$ cm^{-3}. The mass in the equatorial torus is very uncertain, but it could represent a large fraction of the total mass of the envelope.

5. The searchlight beams may result from a preferred illumination of the halo through "holes" excavated in an inner dust cocoon, maybe by the same agent responsible for carving out the bipolar lobes.

6. The intersecting arcs, which are spaced at time intervals ranging between 190 and 250 yr, are reasonably well explained by the binary-induced spiral outflow model originally described by Mastrodemos & Morris (1999), which produces arclike features very similar to those observed in IRAS 18276−1431 for a system viewed nearly edge-on and taking into account illumination effects (M. Morris et al. 2007, in preparation).

7. The analysis of the NIR colors indicates that the scattering nebula is partially illuminated by the central star (with $T_{\rm eff} = 4000$–10,000 K) and partially by a warm ($\sim$300–500 K) dust component. The presence of warm dust is confirmed by modeling of its full SED.

8. We have modeled the 5–100 μm wavelength range of IRAS 18276−1431 using the dust radiative transfer model built in CLOUDY. Based on the detection of a weak 9.7 μm silicate feature, astronomical silicates have been used in our model. The grain size distribution used is the same as that adopted by Gledhill (2005) to explain NIR polarimetry data. The central star has been assumed to emit like a $T_{\rm eff} = 7000$ K, $L = 6400\ L_\odot$ blackbody at a distance $D = 3$ kpc.

9. SED modeling suggests a two-shell structure: (1) an outer dust shell with inner and outer radius $R_{\rm in} \sim 1.6 \times 10^{16}$ and $R_{\rm out} \gtrsim 1.25 \times 10^{17}$ cm, dust temperature $T_{\rm dust} \sim 105$–50 K, and mass-loss rate that increased from $\dot{M} \sim 2 \times 10^{-4}$ to $2 \times 10^{-3}\ M_\odot$ yr^{-1} in $\sim$2000 yr (adopting an expansion velocity $V_{\rm exp} = 17$ km s^{-1}; see below); and (2) an inner shell with $R_{\rm in} \sim 6.3 \times 10^{14}$ cm, $T_{\rm dust} \sim 500$–105 K, and $\dot{M} \sim 3 \times 10^{-5}\ M_\odot$ yr^{-1}.

10. The mass of the envelope enclosed within $R_{\rm out} = 1.25 \times 10^{17}$ cm derived from SED modeling is $\sim$1 $M_\odot$, for a dust-to-gas mass ratio of $\delta = 200$.

11. The molecular envelope of IRAS 18276−1431 is unresolved in our $\sim 8''$ resolution ^{12}CO maps. Our CO data indicate that the bulk of the CO-emitting nebula is expanding at low velocity, $V_{\rm exp} = 17$ km s^{-1}. Adopting a mean kinetic temperature in the envelope of $T_{\rm kin} = 110$ K, as predicted by CLOUDY for the best-fit model to its SED, we derive a mass of $M > 0.38\ M_\odot$ for the molecular envelope.

12. Our best-fit SED model underestimates the observed submillimeter and millimeter flux. This excess can be accounted for by an additional population of big grains (radius $a \gtrsim 0.4$ mm) with temperature and mass in the range $T_{\rm dust} = 150$–20 K and $M_{\rm dust} = (0.16$–$1.6) \times 10^{-3}\ M_\odot$, respectively. The location of this large grain component is unknown, since the 2.6 mm continuum emission is unresolved in our maps. One possibility is that big grains are located in the dense equatorial waist.

Facilities: Keck II (NIRC2), HST (WFPC2), OVRO.

REFERENCES

Alcolea, J., Bujarrabal, V., Sánchez Contreras, C., Neri, R., & Zweigle, J. 2001, A&A, 373, 932
Bains, I., Gledhill, T. M., Yates, J. A., & Richards, A. M. S. 2003, MNRAS, 338, 287
Balick, B. 1987, AJ, 94, 671
Balick, B., & Frank, A. 2002, ARA&A, 40, 439
Bedijn, P. J. 1987, A&A, 186, 136
Bowers, P. F., Johnston, K. J., & Spencer, J. H. 1983, ApJ, 274, 733
Bujarrabal, V., Alcolea, J., Neri, R., & Grewing, M. 1997, A&A, 320, 540
Bujarrabal, V., Alcolea, J., Sánchez Contreras, C., & Sahai, R. 2002, A&A, 389, 271

Bujarrabal, V., Castro-Carrizo, A., Alcolea, J., & Sánchez Contreras, C. 2001, A&A, 377, 868

Draine, B. T., & Lee, H. M. 1984, ApJ, 285, 89

Engels, D. 2002, A&A, 388, 252

Ferland, G. J., Korista, K. T., Verner, D. A., Ferguson, J. W., Kingdon, J. B., & Verner, E. M. 1998, PASP, 110, 761

García-Segura, G., López, J. A., & Franco, J. 2001, ApJ, 560, 928

Gledhill, T. M. 2005, MNRAS, 356, 883

Gürtler, J., Kömpe, C., & Henning, T. 1996, A&A, 305, 878

Hakkila, J., Myers, J. M., Stidham, B. J., & Hartmann, D. H. 1997, AJ, 114, 2043

Herman, J., & Habing, H. J. 1985, A&AS, 59, 523

Heske, A., Forveille, T., Omont, A., van der Veen, W. E. C. J., & Habing, H. J. 1990, A&A, 239, 173

Hrivnak, B. J., & Bieging, J. H. 2005, ApJ, 624, 331

Hrivnak, B. J., Kwok, S., & Su, K. Y. L. 2001, AJ, 121, 2775

———. 1999, ApJ, 524, 849

Jura, M., Turner, J., & Balm, S. P. 1997, ApJ, 474, 741

Knapp, G. R., Bowers, P. F., Young, K., & Phillips, T. G. 1994, ApJ, 429, L33

Knapp, G. R., Sandell, G., & Robson, E. I. 1993, ApJS, 88, 173

Kwok, S., Hrivnak, B. J., & Su, K. Y. L. 2000, ApJ, 544, L149

Latter, W. B., Hora, J. L., Kelly, D. M., Deutsch, L. K., & Maloney, P. R. 1993, AJ, 106, 260

Le Bertre, T. 1987, A&A, 180, 160

Le Bertre, T., Heydari-Malayeri, M., Epchtein, N., Gouiffes, C., & Perrier, C. 1989, A&A, 225, 417

Leggett, S. K., et al. 2003, MNRAS, 345, 144

Martin, P. G., & Rouleau, F. 1991, in Extreme Ultraviolet Astronomy, ed. R. F. Malina & S. C. Bowyer (New York: Pergamon), 341

Mastrodemos, N., & Morris, M. 1999, ApJ, 523, 357

Mauron, N., & Huggins, P. J. 2006, A&A, 452, 257

Meixner, M., et al. 1999, ApJS, 122, 221

Morris, M. 1981, ApJ, 249, 572

Nyman, L.-A., Hall, P. J., & Olofsson, H. 1998, A&AS, 127, 185

Rohlfs, K., & Wilson, T. L. 2000, Tools of Radio Astronomy (New York: Springer)

Sahai, R. 1999, ApJ, 524, L125

Sahai, R., Le Mignant, D., Sánchez Contreras, C., Campbell, R. D., & Chaffee, F. H. 2005, ApJ, 622, L53

Sahai, R., & Sánchez Contreras, C. 2004, in ASP Conf. Ser. 313, Asymmetrical Planetary Nebulae III, ed. M. Meixner et al. (San Francisco: ASP), 32

Sahai, R., & Trauger, J. T. 1998, AJ, 116, 1357

Sahai, R., Young, K., Patel, N. A., Sánchez Contreras, C., & Morris, M. 2006, ApJ, 653, 1241

Sahai, R., et al. 1998, ApJ, 493, 301

Sánchez Contreras, C., Alcolea, J., Bujarrabal, V., & Neri, R. 1998, A&A, 337, 233

Sánchez Contreras, C., Bujarrabal, V., Castro-Carrizo, A., Alcolea, J., & Sargent, A. 2004a, ApJ, 617, 1142

Sánchez Contreras, C., Gil de Paz, A., & Sahai, R. 2004b, ApJ, 616, 519

Sánchez Contreras, C., Le Mignant, D., Sahai, R., Chaffee, F. H., & Morris, M. 2006, in IAU Symp. 234, Planetary Nebulae in Our Galaxy and Beyond, ed. M. J. Barlow & R. H. Méndez (Cambridge: Cambridge Univ. Press), 71

Sánchez Contreras, C., & Sahai, R. 2001, ApJ, 553, L173

———. 2004, in ASP Conf. Ser. 313, Asymmetrical Planetary Nebulae III, ed. M. Meixner et al. (San Francisco: ASP), 377

Soker, N. 2000, ApJ, 540, 436

Su, K. Y. L. 2004, in ASP Conf. Ser. 313, Asymmetrical Planetary Nebulae III, ed. M. Meixner et al. (San Francisco: ASP), 247

Su, K. Y. L., Hrivnak, B. J., & Kwok, S. 2001, AJ, 122, 1525

Su, K. Y. L., Hrivnak, B. J., Kwok, S., & Sahai, R. 2003, AJ, 126, 848

Suh, K.-W. 1999, MNRAS, 304, 389

Szymczak, M., & Gérard, E. 2005, A&A, 433, L29

Tokunaga, A. T., & Vacca, W. D. 2005, PASP, 117, 421

Ueta, T., & Meixner, M. 2003, ApJ, 586, 1338

van der Veen, W. E. C. J., Omont, A., Habing, H. J., & Matthews, H. E. 1995, A&A, 295, 445

van Hoof, P. A. M., Weingartner, J. C., Martin, P. G., Volk, K., & Ferland, G. J. 2004, MNRAS, 350, 1330

Walmsley, C. M., Chini, R., Kreysa, E., Steppe, H., Forveille, T., & Omont, A. 1991, A&A, 248, 555

Wizinowich, P., et al. 2000, PASP, 112, 315

Yusef-Zadeh, F., Morris, M., & White, R. L. 1984, ApJ, 278, 186